

# Comparing different ansatzes to describe electroweak radiative corrections to exclusive semileptonic $B$ meson decays into (pseudo)scalar final state mesons using Monte-Carlo techniques

FLORIAN U. BERNLOCHNER<sup>1</sup>, MAREK SCHÖNHERR<sup>2</sup>

<sup>1</sup> *Institut für Physik, Humboldt Universität Berlin, Germany*

<sup>2</sup> *Institut für Kern- und Teilchenphysik, Technische Universität Dresden, Germany*

## ABSTRACT

In this publication electroweak next-to-leading order corrections to semileptonic  $B$ -meson decays into (pseudo)scalar final states are presented. To this end, these corrections of  $\mathcal{O}(\alpha G_F)$  have been calculated in the QED-enhanced phenomenological model, incorporating the bound-state mesons as its degrees of freedom, and matched to a similar calculation on the level of constituent partons in the full Standard Model. Consequently, the effects arising due to corrections of the partial decay widths on the extraction of the CKM matrix elements  $|V_{cb}|$  and  $|V_{ub}|$  are detailed. Further, the results of two independent Monte-Carlo implementations are presented: One is the dedicated, strict fixed-order generator BLOR, and the other is embedded into the generic Yennie-Frautschi-Suura-type resummation of PHOTONS++, which is part of the multi-purpose event generator SHERPA. The resulting distributions are compared against the standard tool used in many experimental analyses, PHOTOS, showing improvements on the shapes of kinematic distributions of both the lepton and the final state meson.

# Contents

<b>1. Introduction</b>	<b>2</b>
<b>2. Phenomenological model</b>	<b>4</b>
2.1. Tree-level decay revised . . . . .	4
2.2. Next-to-leading order corrections . . . . .	5
2.3. Structure dependent terms . . . . .	10
2.4. Soft-resummation and inclusive exponentiation . . . . .	12
<b>3. Methods &amp; Implementations</b>	<b>13</b>
3.1. BLOR . . . . .	13
3.2. SHERPA/PHOTONS++ . . . . .	13
3.3. PHOTOS . . . . .	14
<b>4. Results</b>	<b>15</b>
4.1. Next-to-leading order corrections to decay rates . . . . .	15
4.2. Next-to-leading order corrections to differential rates . . . . .	18
4.3. Influence of explicit short-distance terms . . . . .	25
<b>5. Conclusions</b>	<b>29</b>
<b>A. Form factor models of exclusive semileptonic <math>B</math> meson decays reviewed.</b>	<b>30</b>
A.1. Form factors for $B \rightarrow D \ell \nu$ . . . . .	30
A.2. Form factors for $B \rightarrow \pi \ell \nu$ . . . . .	30
A.3. Form factors for $B \rightarrow D_0^* \ell \nu$ . . . . .	31
<b>B. Next-to-leading order matrix elements</b>	<b>32</b>

## 1. Introduction

In the Standard Model, the Cabibbo-Kobayashi-Maskawa (CKM) matrix [1, 2] governs the charged current weak interactions between the up- and down-type quarks of the three fermion generations. The precision determination of its matrix elements and its CP-violating complex phase in the  $B$  meson sector has been the focus of intense research over the past decade. The combination of various measurements to test the unitarity of the CKM matrix is considered a strong instrument in the search for physics beyond the Standard Model [3, 4].

In the present paper, a calculation of the electroweak next-to-leading order corrections in exclusive semileptonic  $B$  meson decays into (pseudo)scalar mesons,  $B \rightarrow D \ell \nu_\ell$ ,  $B \rightarrow D_0^* \ell \nu_\ell$  and  $B \rightarrow \pi \ell \nu_\ell$ ,  $\ell$  denoting either an electron or a muon, is presented. Next-to-leading order corrections to such decays are an important aspect in the extraction of the CKM matrix elements  $|V_{cb}|$  and  $|V_{ub}|$  at  $B$ -factory experiments. Virtual electroweak bosons running in the loop as well as real photon emissions off all charged particles present in the decay alter the resulting decay dynamics and enhance the weak decay rate. To correct for the changed decay dynamics, experimentalists use approximative all-purpose next-to-leading order algorithms. These exploit universal factorisation theorems in the soft and/or collinear photon energy limit [5–7]. In addition, the total hadronic decay rate of semileptonic decays are corrected by the known leading logarithm of the virtual corrections of the partonic decay [8, 9].

Experience from exclusive semileptonic  $K$  meson decays illustrate the importance of having a good understanding of such radiative effects: until 2004 the global average of the extracted value of  $|V_{us}|$  from  $K_{l3}^+$  and  $K_{l3}^0$  decays implied the violation of CKM unitarity by two standard deviations [10]. Further measurements proved dissonant with these findings [11–14], indicating that the achieved experimental precision needed an improved understanding of electroweak corrections. Since for many decays next-to-leading order calculations do not exist, experiments often use the approximative all-purpose algorithm PHOTOS [15,16] to study the reconstruction efficiency and acceptance. The accuracy of this approach was tested by the KTeV collaboration, using the measured photon spectra from radiative  $K_{l3}^0$  decays: the angular distribution of the simulated photons did not agree well with the predicted spectrum [17]. This led to the development of the next-to-leading order Monte Carlo generator KLOR (see [17]), whose next-to-leading order calculation is based on a phenomenological model. Its predicted angular photon distribution agreed satisfactorily with the measured spectra. Although this approach is very precise, it is also the most complicated one to adopt for an experiment: electroweak next-to-leading order calculations only exist for a few decay modes, sometimes only valid in a limited region of phase-space. Most of these calculations are evaluated numerically and rely on customised Monte Carlo generators.

Over the last 10 years, an increasing amount of data and a better understanding of detector effects lead to a very accurate picture of physics at the  $B$ -factory experiments. This increased precision then led to the demand of knowledge of next-to-leading order electroweak effects beyond the precision of approximative all-purpose algorithms. The present paper aims at improving the status quo by providing a prediction for both total decay rates and differential distributions of a few representative kinematic variables. For the latter the predictions of a dedicated Monte-Carlo generator, BLOR [18], is compared to two all-purpose generators, SHERPA/PHOTONS++ [19,20] and PHOTOS [15,16]. While the latter is a QED-parton-shower Monte Carlo program intended to supplement generic leading logarithmic corrections to pure leading order decay generators, the former is a full-fledged hadron-level Monte Carlo generator for collider physics whose internal leading order (hadronic) decays are supplemented by a universal soft-photon-resummation systematically improved, where possible, by known exact next-to-leading order matrix elements. While the improved description of inclusive decay rates directly gives small corrections to the extracted values of  $|V_{cb}|$  and  $|V_{ub}|$  from semileptonic decays, the improved description of the decay kinematics influence extrapolation to corners of the phase space and, therefore, leads to both direct and indirect corrections.

The considerations of the present paper proceed as follows: Sec. 2.1 briefly reviews exclusive  $B \rightarrow X \ell \nu_\ell$  decays at tree-level. Thereafter, Sec. 2.2 develops the next-to-leading order formalism, reviewing both the partonic short-distance results of [8,9], the hadronic long-distance QED-improved effective decay and their matching to one-another, including also a detailed discussion on non-universal structure-dependent terms in Sec. 2.3. This model is then embedded into the resummation in the soft limit of Yennie, Frautschi and Suura [6] in Sec. 2.4. Sec. 3 then shortly reviews the basic principles of both BLOR and SHERPA/PHOTONS++ where the calculations of Sec. 2 have been implemented, and of PHOTOS. The total inclusive decay rates obtained are shown in Sec. 4.1 while differential distributions are shown in Sec. 4.2, also detailing the improvement over the current estimates. The influence of the structure-dependent terms, where known, on the results is presented in Sec. 4.3. Sec. 5 finally summarises the results.

Note that the charge-conjugated modes are implied throughout the present paper.

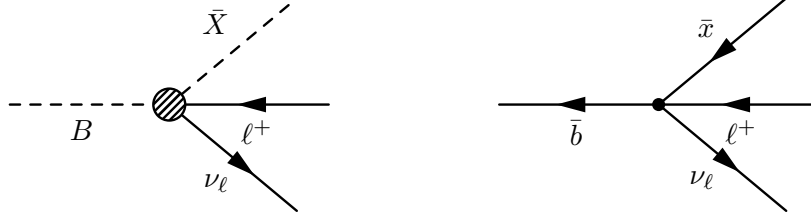


**Fig. 1** The tree-level weak  $B \rightarrow \bar{X} \ell^+ \nu_\ell$  decay is shown both in the phenomenological picture (left) and, at parton level, in Fermi's theory as low energy approximation of the Standard Model (right). The shaded circle represents the effective vertex parametrised by form factors  $f_\pm$ ,  $x \in \{u, c\}$ .

## 2. Phenomenological model

### 2.1. Tree-level decay revised

The phenomenological interaction Lagrangian of the weak  $B \rightarrow X \ell \nu$  decay to a (pseudo)scalar final state in Fermi's theory, with constant form factors of the hadronic current,  $f_\pm$ , is given by

$$\mathcal{L}_W = \frac{G_F}{\sqrt{2}} V_{xb} [(f_+ + f_-) \phi_X \partial^\mu \phi_B + (f_+ - f_-) \phi_B \partial^\mu \phi_X] \bar{\psi}_\nu P_R \gamma_\mu \psi_\ell + \text{h.c.}, \quad (2.1)$$

where  $\psi_\ell$  and  $\psi_\nu$  are the Dirac fields of the lepton and the neutrino,  $\phi_B$  and  $\phi_X$  are the scalar fields of the initial and final state mesons,  $G_F$  the Fermi coupling,  $V_{xb}$  the CKM matrix element governing the strength of the  $b \rightarrow x$  transition, and  $P_R = 1 + \gamma_5$  is derived from the right-handed projection operator by absorbing the factor  $\frac{1}{2}$  into the coupling definition. The Lagrangian of eq. (2.1) leads to the transition matrix element<sup>1</sup>

$$\mathcal{M}_0^0 = -i \frac{G_F}{\sqrt{2}} V_{xb} H_\mu(p_B, p_X; t) \bar{u}_\nu P_R \gamma^\mu v_\ell, \quad (2.2)$$

with the hadronic current, generalised to variable form factors,

$$H_\mu(p_B, p_X; t) = \langle X | \bar{\psi}_x P_R \gamma_\mu \psi_b | B \rangle = (p_B + p_X)_\mu f_+(t) + (p_B - p_X)_\mu f_-(t). \quad (2.3)$$

The four-momenta labels in eq. (2.2) are introduced in Fig. 1. The generalised form factors  $f_\pm = f_\pm(t)$  now describe the phase-space dependent influence of the strong interaction on the weak decay dynamics and are functions of the squared momentum transfer from the hadronic to the leptonic system only, given at tree-level by

$$t = (p_B - p_X)^2 = (p_\ell + p_\nu)^2. \quad (2.4)$$

The tree-level differential decay rate in the  $B$ -meson rest frame is then given by

$$d\Gamma_0^0 = \frac{1}{64 \pi^3 m_B} |\mathcal{M}_0^0|^2 dE_X dE_\ell, \quad (2.5)$$

with  $E_X = p_X^0$  and  $E_\ell = p_\ell^0$ . The explicit expressions of the  $f_\pm(t)$  as function of the momentum transfer squared for the processes considered in this paper,  $B \rightarrow D \ell \nu$ ,  $B \rightarrow D_0^* \ell \nu$  and  $B \rightarrow \pi \ell \nu$ , can be found in App. A.

<sup>1</sup>Throughout this paper  $\mathcal{M}_m^n$  denote a matrix element at  $\mathcal{O}(G_F \alpha^n)$  with  $m$  photons in the final state. The total decay rate at  $\mathcal{O}(G_F \alpha^n)$  is denoted as  $\Gamma_m^n$ .

## 2.2. Next-to-leading order corrections

The arising electroweak next-to-leading order corrections can be divided into two energy regimes: short-distance corrections at parton level, and long-distance corrections within the phenomenological model. First, Sec. 2.2.1 will discuss how both descriptions can be matched and renormalised. Sec. 2.2.2 then reviews the calculation of the virtual short-distance corrections of [8,9]. The long-distance corrections, following from an extension of the phenomenological model, are then discussed in Sec. 2.2.3.

### 2.2.1. Matching of different energy regimes

The aim of this section is to develop a formalism to calculate the corrections at  $\mathcal{O}(\alpha G_F)$ . The standard approach involves calculating the one-loop graphs for the  $B \rightarrow X \ell \nu_\ell$  decay in the effective theory with counterterms and compare it to the renormalised Standard Model result. Fixing the counterterms results in the desired matching of both results. The effective theory itself is non-renormalisable, but the Standard Model can be renormalised to measured quantities, e.g. the Fermi coupling constant of the muon decay, the electron mass, and the fine-structure constant, in order to produce finite predictions. Such a matching procedure was carried out in great detail by [21] for semileptonic Kaon decays where the leading order phenomenological decay is described by a chiral Lagrangian.

In the present paper, however, an alternative route is pursued. Consider a general logarithmically divergent  $N$ -point tensor integral of rank  $p$  with a single massless photon propagator. It can be cast in the form

$$T^{\mu_1 \dots \mu_p}(p_1, \dots, p_{N-1}) \propto \int d^4k \frac{k^{\mu_1} \dots k^{\mu_p}}{k^2 d_1 \dots d_{N-1}}, \quad (2.6)$$

with denominators  $d_i = (p_i - k)^2 - m_i^2$ . The integral can then be split according to

$$\begin{aligned} T^{\mu_1 \dots \mu_p}(p_1, \dots, p_{N-1}) \propto & \int d^4k \left[ \frac{k^{\mu_1} \dots k^{\mu_p}}{k^2 d_1 \dots d_{N-1}} - \frac{k^{\mu_1} \dots k^{\mu_p}}{[k^2 - \Lambda^2] d_1 \dots d_{N-1}} \right] \\ & + \int d^4k \frac{k^{\mu_1} \dots k^{\mu_p}}{[k^2 - \Lambda^2] d_1 \dots d_{N-1}}. \end{aligned} \quad (2.7)$$

This amounts to regulating the ultraviolet behaviour of the first term using an unphysical photon-like vector field of mass  $\Lambda$  and opposite norm, as proposed by Pauli and Villars in [22]. Its infrared behaviour is left unchanged, thus, relying on the Kinoshita-Lee-Nauenberg theorem [23, 24], these divergences are left to be canceled by the real corrections. The second term of eq. (2.7) is the equivalent of eq. (2.6), this time only with a massive photon. Hence, it is infrared finite and possesses the identical ultraviolet behaviour.

Transferring this observation to the present case of semileptonic  $B$  meson decays where, both in the effective theory and in the Standard Model, there is at most one massless photon propagator in any one-loop diagram, the virtual emission matrix element can be decomposed as

$$\mathcal{M}_0^1 = \mathcal{M}_{0,\text{ld}}^1(\Lambda) + \mathcal{M}_{0,\text{sd}}^1(\Lambda). \quad (2.8)$$

The term  $\mathcal{M}_{0,\text{ld}}^1$  is now comprised of the Pauli-Villars regulated exchange of a massless photon, including its infrared divergence. The specific UV regulator effectively restricts the virtual photon's momentum to be smaller than  $\Lambda$ . Hence, it describes long-distance (ld) interactions only.

The term  $\mathcal{M}_{0,\text{sd}}^1$ , on the other hand, carries the full ultraviolet behaviour of  $\mathcal{M}_0^1$ . It thus can be used for renormalising all parameters. Consequently, because eq. (2.7) is exact, all parameters in

$\mathcal{M}_{0,\text{ld}}^1$  are then renormalised automatically. Through the photon mass, its virtual propagator's momentum is effectively restricted to be larger than  $\Lambda$ . Hence, this term describes the short-distance (sd) interactions only.

The above is exact as long as the same Lagrangian input is used to calculate both the short-distance and the long-distance parts. In practice, however, due to the confining, non-perturbative nature of QCD this is not feasible for the processes at hand. For scales larger than the hadron mass, its parton content can be resolved, electroweak corrections have to be calculated on the basis of (constituent) quarks. For scales smaller than the hadron mass, its parton content cannot be resolved, the bound-state hadrons themselves are the relevant degrees of freedom. Thence, supposing  $\Lambda$  is set such, that it effectively separates those two regimes, the long-distance QED corrections  $\mathcal{M}_{0,\text{ld}}^1$  can be calculated using the phenomenological model and for the short-distance corrections  $\mathcal{M}_{0,\text{sd}}^1$  the full Standard Model has to be invoked. This is justified, in principle, by the assumption, that the phenomenological model describes the Standard Model and its effective degrees of freedom at these low scales. This mere fact, however, directly leads to inconsistencies at the matching scale  $\Lambda$ , where both models should give the same answer. Thus, this matching is only approximate and the associated systematic uncertainties to this method can be estimated by varying the matching parameter, cf. Sec. 4.1.

The above reasoning leads to an optimal value for  $\Lambda$ : the smallest hadronic mass in the decay. Then, only low-energy virtual photons, not able to resolve either of both mesons, are described by the effective theory, while high-energy virtual photons are described by the short-distance picture of the full Standard Model, resolving the partonic content of both the charged and the neutral meson involved. Further, as long as  $\Lambda > E_\gamma^{\text{max}}$ , the kinematic limit of the photon energy in single photon emission<sup>2</sup>, the real emission of photons off these charged mesons are also correctly described by the phenomenological model (except for structure dependent terms discussed in Sec. 2.3).

Nonetheless, it has to be noted that there are conceptual problems if both hadronic scales differ significantly. Then, there is a large intermediate regime, where virtual photons are able to resolve one meson, but not the other. By the above choice of  $\Lambda$  it is expected to give the best approximate description in this region. Further, if the third scale  $E_\gamma^{\text{max}}$  exceeds  $\Lambda$ , real radiation, in the present ansatz always described using the phenomenological model, is able to resolve the final state meson, be it charged or neutral, as well. However, even if a considerable fraction is radiated at scales above  $\Lambda$ , this should have only negligible effects on the total decay rate as the bulk of the radiation is in the region  $k \rightarrow 0$  and, therefore, adequately described.

### 2.2.2. Short-distance next-to-leading order corrections

The well-known Standard Model Lagrangian is used in this study to describe the partonic  $b \rightarrow x \ell \nu$  decay in the short-distance regime. A representative collection of relevant next-to-leading order corrections to the tree-level decay, involving the exchange of virtual photons,  $W$  and  $Z$  bosons as well as Higgs scalars, is depicted in Fig. 2. Besides vertex corrections to the  $b$ - $x$ - $W$  and  $\ell$ - $\nu$ - $W$  vertices, wave function and propagator corrections, box diagrams involving the additional exchange of a neutral  $\gamma$ ,  $Z$  or  $h$  bosons between the hadronic and leptonic systems are present. These next-to-leading order corrections read, calculated in [8] within the current algebra framework and concentrating on the renormalisation of the bare Fermi coupling  $\hat{G}_F$  for

---

<sup>2</sup> The maximum photon energy for single photon radiation in the rest frame of a decaying particle is half its mass, neglecting all other decay products' masses. Allowing for massive decay products further reduces this kinematic limit.

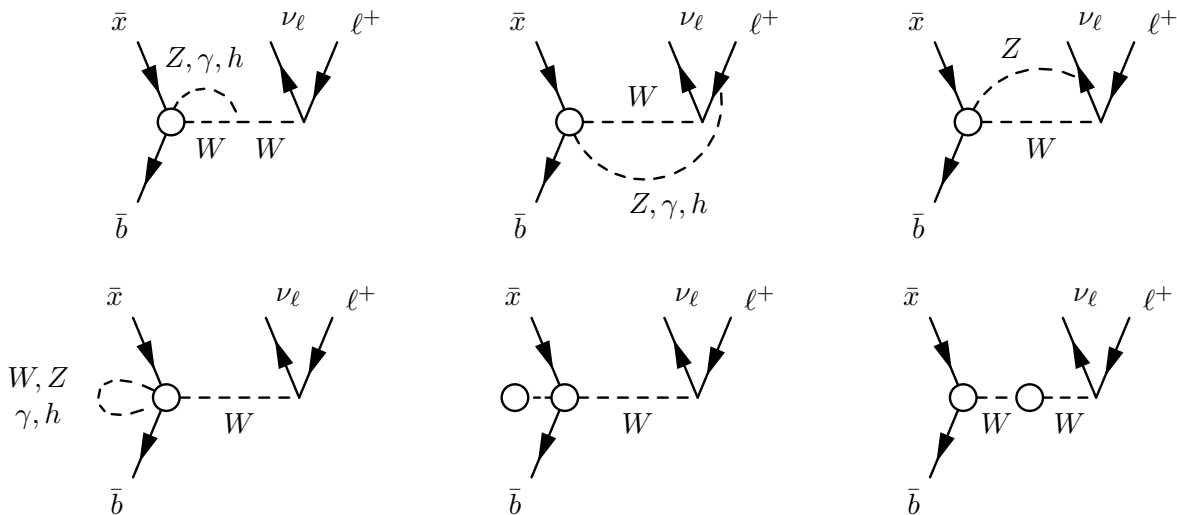


**Fig. 2** Representative Feynman diagrams of the Standard Model partonic decay  $\bar{b} \rightarrow \bar{x} \ell^+ \nu_\ell$  are shown. The white circles indicate hadronic contributions that are neglected in the short-distance expansion.

this process, to leading logarithmic accuracy

$$\hat{\mathcal{M}}_{0,\text{sd}}^1(\Lambda) = \frac{\alpha \hat{G}_F}{4\pi} \left[ 3 \ln \frac{m_W}{\Lambda} + 6\bar{Q} \ln \frac{m_W}{\Lambda} - 3\bar{Q} \ln \frac{m_W^2}{m_Z^2} + \dots \right] \tilde{\mathcal{M}}_0^0, \quad (2.9)$$

with  $\hat{\mathcal{M}}_0^0 = \hat{G}_F \tilde{\mathcal{M}}_0^0$ , i.e. the leading order matrix element stripped of the Fermi coupling constant, and  $\bar{Q}$  being the average charge of the quark line. The ellipsis stands for non-logarithmic terms. For the photonic contributions an infrared regulator has been introduced in the form of a photon mass  $\Lambda \ll m_W$ . Thus, the resulting matrix element has exactly the form required for the matching outlined in Sec. 2.2.1. The arising loop corrections are ultraviolet (UV) divergent and have been regularised in [8] by a UV cutoff set to  $m_W$ . Renormalisation of the parameters, again focusing on  $\hat{G}_F$ , is then achieved by comparison to the muon decay computed in the same computational framework, yielding the relation

$$G_F = \hat{G}_F \left[ 1 + \frac{3\alpha}{8\pi} \ln \frac{m_W^2}{m_Z^2} + \dots \right], \quad (2.10)$$

where  $G_F$  is now the renormalised Fermi decay constant as measured in the muon decay. This leads to the partonic short-distance virtual matrix element in the renormalised theory

$$\begin{aligned} \mathcal{M}_{0,\text{sd}}^1(\Lambda) &= \frac{\alpha G_F}{4\pi} \left[ 3 \ln \frac{m_W}{\Lambda} + 6\bar{Q} \ln \frac{m_W}{\Lambda} - \frac{3}{2} (1 + 2\bar{Q}) \ln \frac{m_W^2}{m_Z^2} + \dots \right] \tilde{\mathcal{M}}_0^0 \\ &= \frac{3\alpha}{4\pi} (1 + 2\bar{Q}) \ln \frac{m_Z}{\Lambda} \cdot \mathcal{M}_0^0, \end{aligned} \quad (2.11)$$

where  $G_F$  has been reabsorbed into the leading order matrix element  $\mathcal{M}_0^0$ . In the case of semileptonic  $B$  decays  $\bar{Q} = \frac{1}{2} |Q_{\bar{b}} + Q_{\bar{x}}| = \frac{1}{6}$ ,  $x \in \{u, c\}$ , this gives

$$\mathcal{M}_{0,\text{sd}}^1(\Lambda) = \frac{\alpha}{\pi} \ln \frac{m_Z}{\Lambda} \cdot \mathcal{M}_0^0 + \dots \quad (2.12)$$

The logarithm in eq. (2.12) then represents the leading logarithmic corrections to  $\mathcal{O}(\alpha G_F)$  due to virtual particle exchange with (virtual) photon energies above  $\Lambda$ .

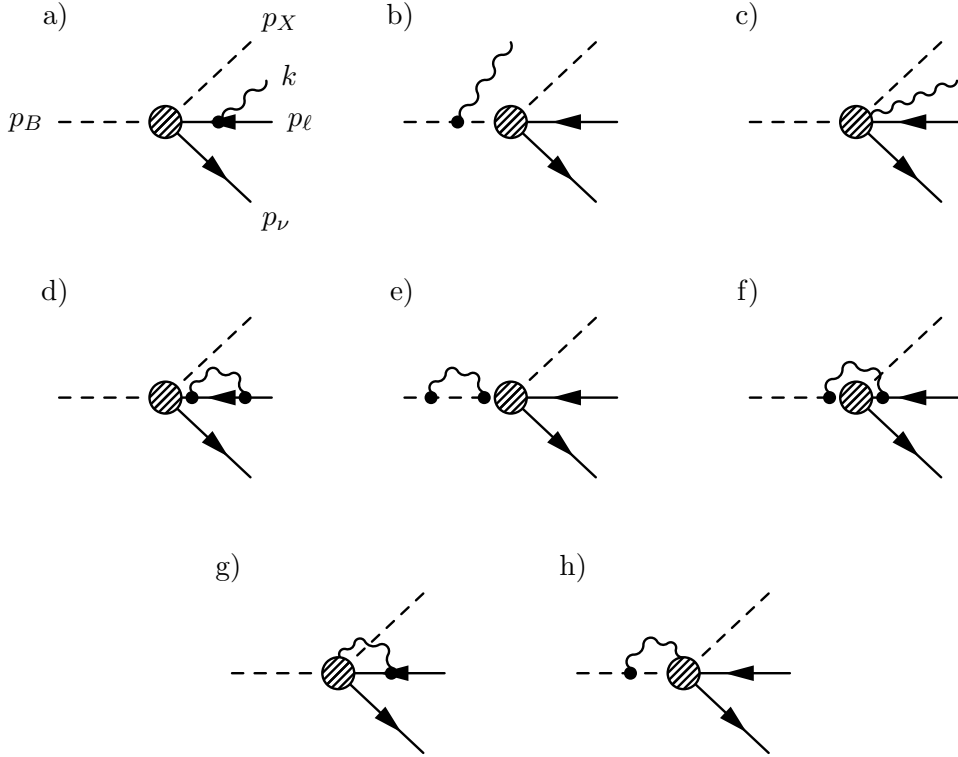


**Fig. 3** The Feynman diagrams for the next-to-leading order corrections to  $B^+ \rightarrow \bar{X}^0 \ell^+ \nu$  decays are shown.

### 2.2.3. Long-distance next-to-leading order corrections

The QED long-distance corrections to the phenomenological hadron decay can be calculated in an effective model that arises by requiring the phenomenological Lagrangian of the leading order decay to be invariant under local  $U(1)_{\text{em}}$  gauge transformations. Assigning the usual charges the following interaction terms in the Lagrangian arise in addition to eq. (2.1)

$$\begin{aligned} \mathcal{L}_{\text{int,QED}} = & -eQ_\ell \bar{\psi}_\ell \gamma^\mu \psi_\ell A_\mu - ieQ_\phi A_\mu (\phi^+ \partial^\mu \phi^- - \phi^- \partial^\mu \phi^+) + e^2 Q_\phi^2 A_\mu A^\mu \phi^+ \phi^- \\ & + ie\sqrt{2}G_F V_{xy} f_\pm (Q_B \pm Q_X) \phi_B \phi_X A_\mu \bar{\psi}_\nu P_R \gamma^\mu \psi_\ell + \text{h.c.} \quad , \end{aligned} \quad (2.13)$$

wherein the summation over  $\phi \in \{\phi_B, \phi_X\}$  is implied. In addition to the point-like lepton-photon and meson-photon interactions, a vertex emission term arises. This term is connected to the bound-state nature of the meson. It is infrared finite and needed for gauge invariance. Further, in eq. (2.13) it is assumed that the meson-photon interaction is sufficiently described by scalar QED. Additional terms arise when moving away from this assumption, including intermediate lines of excited hadrons necessitating  $X^* \rightarrow X\gamma$  vertices as well as contributions due to off-shell currents. These terms are discussed on general grounds in Sec. 2.3 and will be largely neglected in this study. This, in most cases, roots in their unavailability or, where known, in their smallness.

Figs. 3 and 4 depict the relevant real and virtual diagrams for  $B^+ \rightarrow \bar{X}^0 \ell^+ \nu$  and  $B^0 \rightarrow X^- \ell^+ \nu$  decays at  $\mathcal{O}(\alpha G_F)$ . The real corrections diagrams a, b and c correspond to the emission of a real photon from either the charged legs of the decay, or the charged vertex itself. The virtual corrections group into three categories: diagrams d and e concern the wave-function renormalisation of the charged legs while diagram f is the dominant inter-particle photon exchange. Diagrams



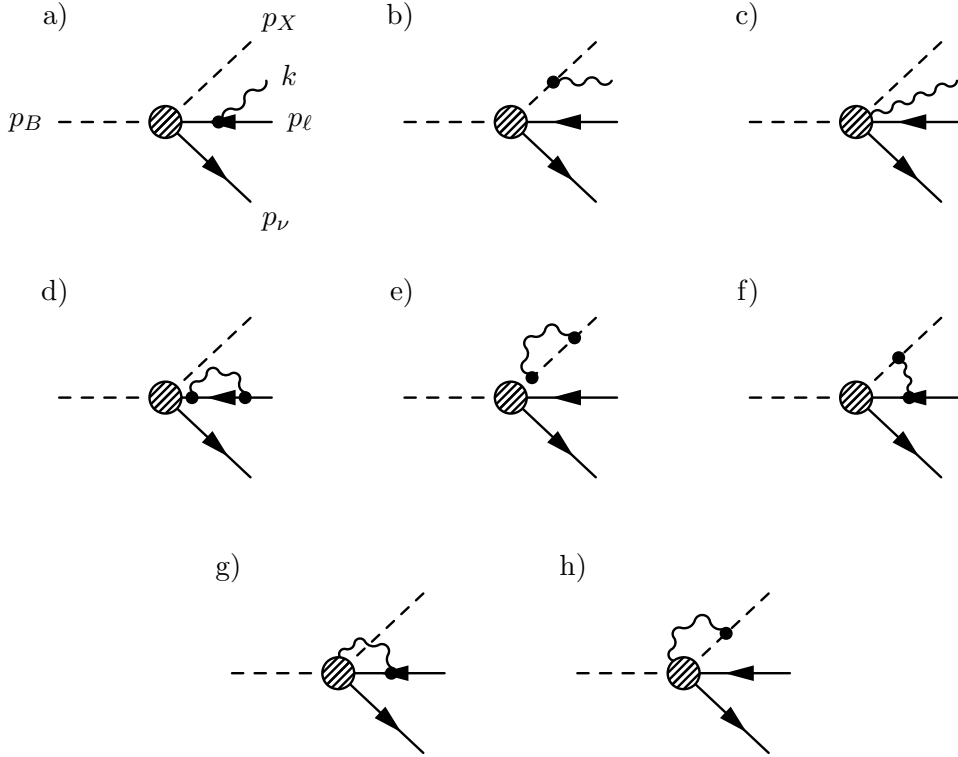


**Fig. 4** The Feynman diagrams for the next-to-leading order corrections to  $B^0 \rightarrow X^- \ell^+ \nu$  decays are shown.

g and h are again due to emissions off the charged effective vertex and are, thus, infrared finite. The corresponding subtleties involving the vertex emissions are detailed in App. B.

In the virtual amplitude  $\mathcal{M}_{0,\text{ld}}^1$  the arising ultraviolet divergences are regularised using the Pauli-Villars prescription [22] by introducing an unphysical heavy photon of mass  $\Lambda$  and opposite norm. Consequently, the virtual corrections have exactly the form required by the matching procedure outlined in Sec. 2.2.1 and all real emission processes are described in the long-distance picture.

Squaring the phenomenological real and virtual matrix elements results in the real and virtual next-to-leading order differential rates. In the  $B$  meson rest frame they read

$$\begin{aligned}
 d\Gamma_1^1 &= \frac{1}{(2\pi)^{12}} \frac{d^3 p_X}{E_X} \frac{d^3 p_\ell}{E_\ell} \frac{d^3 p_\nu}{E_\nu} \frac{d^3 k}{E_k} \delta^{(4)}(p_B - p_X - p_\ell - p_\nu - k) |\mathcal{M}_{1,\text{ld}}^{\frac{1}{2}}|^2, \\
 d\Gamma_0^0 + d\Gamma_0^1 &= \frac{1}{64 \pi^3 m_B} \left( |\mathcal{M}_0^0|^2 + 2\mathcal{R}e[\mathcal{M}_0^0 \mathcal{M}_{0,\text{ld}}^{1*}(\Lambda)] + 2 |\mathcal{M}_0^0|^2 \frac{\alpha}{\pi} \ln \frac{m_Z}{\Lambda} \right) dE_X dE_\ell. \quad (2.14)
 \end{aligned}$$

Integrating eqs. (2.14) results in the next-to-leading order total decay rate. Comparing with the total tree-level decay rate, the integral over phase-space of eq. (2.5), yields the long-distance enhancement factor  $\delta_{\text{ld}}$  due to next-to-leading order effects. It is

$$\Gamma = (1 + \delta_{\text{sd}} + \delta_{\text{ld}}) \Gamma_0^0 = \Gamma_0^0 + \Gamma_0^1 + \Gamma_1^1 + \mathcal{O}(\alpha^2 G_F). \quad (2.15)$$

with  $\delta_{\text{sd}} = \frac{2\alpha}{\pi} \ln \frac{m_Z}{\Lambda}$  from eq. (2.12). The exact form of the next-to-leading order matrix elements can be found in App. B.

### 2.3. Structure dependent terms

This section discusses the arising additional electromagnetic next-to-leading order corrections that cannot be grasped by simply replacing  $\partial_\mu \rightarrow D_\mu$  to arrive at a  $U(1)_{\text{em}}$  gauge invariant phenomenological Lagrangian, as was described in the previous section. These include both deviations arising from the point-like meson-photon interaction assumed above and additional terms arising in the interaction of an off-shell hadronic current. Nonetheless, it is clear that in the relevant phase space region for the total inclusive decay rate, namely the region as  $k \rightarrow 0$  near the infrared divergence, both the real and virtual next to leading order matrix elements are completely determined by the leading order decay, and the above procedure accurately reproduces the full theory in this region [5, 6, 25]. Hence, the real emission squared amplitude in this limit reads

$$|\mathcal{M}_1^{\frac{1}{2}}|^2 \stackrel{k \rightarrow 0}{=} -e^2 \left( \frac{p_M}{k \cdot p_M} - \frac{p_\ell}{k \cdot p_\ell} \right)^2 |\mathcal{M}_0^0|^2 \quad \text{with } p_M \in \{p_B, p_X\}, \quad (2.16)$$

depending on whether  $B$  or  $X$  is charged. Physically this roots in the fact that the wavelength of an infinitely soft photon is much larger than the size of any strongly bound hadron. It, thus, cannot resolve its substructure and effectively interacts with its summed, then point-like charge. Further, such soft photons cannot push the hadronic current significantly off-shell, such that off-shell current interactions can become sizeable.

Introducing non-point-like meson-photon interactions does not only lead to corrections due to the hadron's size and its internal charge distribution, it also leads to additional vertices of the type  $X \rightarrow X^* \gamma$ , where  $X^*$  is a higher resonance of the  $X$  meson. This necessarily also introduces additional terms in the interaction of the hadronic and the leptonic current, especially if the resonance differs in its spin.  $B^*$  resonances in the initial state occur in the unphysical region. Hence, they are only relevant if their width is comparable to, or larger than, the mass separation  $m_B^2 - m_{B^*}^2$  to the initial state  $B$  meson. In contrast,  $D^*$  resonances, for example, occurring in a final state line are allowed to be on-shell for a range of photon energies. Thus, a considerable correction may arise. [26] find the  $D^{*+} \rightarrow D^+ \gamma$  coupling to be compatible with zero while the  $D^{*0} \rightarrow D^0 \gamma$  coupling is small, but considerable. Both are considered and discussed in detail in Sec. 4.3.

Generally, following the argumentation of [27, 28] the electromagnetic current of the hadronic system can be split into two components: *inner-bremsstrahlung* (IB) contributions, which account for photon radiation from the external charged particles and are completely determined by the non-radiative process, and *structure-dependent* (SD) contributions, which describe intermediate hadronic states and represent new information with respect to the IB contributions.

The amplitude of a semileptonic  $B$  meson decay with full electromagnetic corrections reads

$$\mathcal{A}_\nu = i e \frac{G_F}{\sqrt{2}} V_{\text{xb}} \bar{u}_\nu P_R \gamma^\mu \left( -\frac{H_\mu}{2p_\ell \cdot k} (\gamma_\nu \not{k} + 2p_{\ell,\nu}) + V_{\mu\nu} - A_{\mu\nu} \right) v_\ell, \quad (2.17)$$

with the hadronic current  $H_\mu$ , as introduced in eq. (2.3). The hadronic vector and axial form factors of the photon-emitting hadronic current, incorporating among others the  $X \rightarrow X^* \gamma$  coupling, are given by the unknown non-local operator

$$V_{\mu\nu} - A_{\mu\nu} = \int d^4x e^{ik \cdot x} \langle X | T [\hat{h}_\mu(0) J_\nu^{\text{em}}(x)] | B \rangle. \quad (2.18)$$

$J_\nu^{\text{em}}$  denotes the electromagnetic current,  $\hat{h}_\mu$  the quark-current in position-space and  $k$  is the photon momentum. The vector and axial-vector operators of eq. (2.18) obey the electromagnetic

Ward-identities, obtained by contracting  $k^\nu A_\nu$  of eq. (2.17),

$$\begin{aligned} k^\nu V_{\mu\nu} &= H_\mu, \\ k^\nu A_{\mu\nu} &= 0. \end{aligned} \tag{2.19}$$

These properties of the individual pieces of the amplitude in conjunction with Low's theorem [5,25] lead to the fact, that the leading terms of next-to-leading order amplitude in powers of the photon four-momentum  $k$ , i.e. the terms proportional to  $k^{-1}$  and  $k^0$ , are completely determined by the on-shell form factors of the tree-level decay.

Following [27], corrections beyond  $\mathcal{O}(k^0)$  can be included by separating the non-local operator eq. (2.18) into SD and IB contributions. Since the IB and SD describe different physical mechanisms they are separately gauge invariant. Further, the SD amplitude must be of  $\mathcal{O}(k)$  or higher. This, however, does not prevent the IB amplitude from containing terms of  $\mathcal{O}(k)$  and higher as well.

Splitting the amplitude under these restrictions allows more terms to be collected in the IB part, still using only the knowledge of the non-radiative matrix element. This offers the advantage to obtain more precise predictions for the decay process, without formulating the (mostly unknown) SD contributions. The splitting of the transition matrix element requires a corresponding splitting of the non-local operator eq. (2.18) into SD and IB parts.

The axial contributions are strictly zero for photons emitted from the  $B$ - or  $X$ -meson, and therefore can be considered purely SD. They can be written in the form [29]

$$\begin{aligned} A_{\mu\nu} = A_{\mu\nu}^{\text{SD}} &= -i \epsilon_{\mu\nu\rho\sigma} \left[ A_1 p_X^\rho k^\sigma + A_2 k^\rho (p_\ell + p_\nu)^\sigma \right] \\ &\quad - i \epsilon_{\nu\lambda\rho\sigma} p_X^\lambda k^\rho (p_\ell + p_\nu)^\sigma \left[ A_3 (p_\ell + p_\nu)_\mu + A_4 p_\mu \right]. \end{aligned} \tag{2.20}$$

Note that the Lorentz-invariant scalars  $A_i$  are non-singular in the limit  $k \rightarrow 0$  by construction and are functions of the three independent scalar variables that can be built with  $p_B$ ,  $p_X$  and  $k$ . The decomposition of the vector current reads

$$V_{\mu\nu} = V_{\mu\nu}^{\text{IB}} + V_{\mu\nu}^{\text{SD}}, \tag{2.21}$$

where the IB piece is chosen in such a way, that

$$\begin{aligned} k^\nu V_{\mu\nu}^{\text{IB}} &= H_\mu \\ k^\nu V_{\mu\nu}^{\text{SD}} &= 0. \end{aligned} \tag{2.22}$$

Thus, the decay amplitude separates as

$$\begin{aligned} \mathcal{A}_\nu &= i e \frac{G_F}{\sqrt{2}} V_{\text{xb}} \bar{u}_\nu P_R \gamma^\mu \left( -\frac{H_\mu}{2p_\ell \cdot k} (\gamma^\rho k + 2p_\ell^\rho) + V_{\mu\nu}^{\text{IB}} \right) v_\ell \\ &\quad + i e \frac{G_F}{\sqrt{2}} V_{\text{xb}} \bar{u}_\nu P_R \gamma^\mu (V_{\mu\nu}^{\text{SD}} - A_{\mu\nu}^{\text{SD}}) v_\ell. \end{aligned} \tag{2.23}$$

Herein,  $V_{\mu\nu}^{\text{IB}}$  can be constructed from leading order information only, cf. App. B. The SD vector contributions, on the other hand, contain additional information. They can be written as [30]

$$\begin{aligned} V_{\mu\nu}^{\text{SD}} &= V_1 \left[ k_\mu p_{X\nu} - (p \cdot k) g_{\mu\nu} \right] + V_2 \left[ k_\mu (p_\ell + p_\nu)_\nu - (k \cdot (p_\ell + p_\nu)) g_{\mu\nu} \right] \\ &\quad + V_3 \left[ (k \cdot (p_\ell + p_\nu)) (p_\ell + p_\nu)_\mu p_{X\nu} - (p_X \cdot k) (p_\ell + p_\nu)_\mu (p_\ell + p_\nu)_\nu \right] \\ &\quad + V_4 \left[ (k \cdot (p_\ell + p_\nu)) (p_{X\mu} p_{X\nu} - (p_X \cdot k) p_{X\mu} (p_\ell + p_\nu)_\nu) \right], \end{aligned} \tag{2.24}$$

where the Lorentz-invariant scalars  $V_i$  are functions of the three independent scalar variables that can be built with  $p_B, p_X$  and  $k$ . All IB and SD contributions are finite as  $k \rightarrow 0$ . The IB and SD parametrization of [31] based on [32] can be obtained by a change of basis in eq. (2.24), and correspondingly shifting terms of  $\mathcal{O}(k)$  and higher into the SD contributions. The IB coupling to the electromagnetic current can be used to construct the next-to-leading order matrix elements, receiving in principle additional corrections from the SD coupling.

The knowledge of the full SD contributions for semileptonic  $B$  meson decays is modest: [31] discusses the matter for  $B \rightarrow \pi \ell \nu \gamma$  decays, using the soft-collinear effective theory to isolate the expressions for the SD contributions in the soft-pion and hard-photon part of phase-space. Sec. 4.3 compares their findings with the pure IB result from this study. The differences are non sizable. The recent work of [28] addresses the real SD corrections to  $B \rightarrow D \ell \nu \gamma$  decays by using lattice results of the  $D^* \rightarrow D \gamma$  coupling to estimate the dominant SD contributions when the  $D^*$  is on-shell. Sec. 4.3 also compares these SD contribution with the complete SD+IB picture. Again the differences turn out to be non sizable. The SD corrections to  $B \rightarrow D_0^* \ell \nu \gamma$  are unknown, but given the large widths of the  $D_0^*$  and  $D_1^*$  states a non-negligible correction to the pure IB prediction can be expected.

## 2.4. Soft-resummation and inclusive exponentiation

This section discusses a systematic improvement of the fixed order results discussed in the previous section. Centring on the exponentiability of soft-radiative corrections and following the approach of Yennie, Frautschi and Suura [6], the fully inclusive decay rate

$$\Gamma = \frac{1}{2M} \sum_{n_R=0}^{\infty} \frac{1}{n_R!} \int d\Phi_{p_f} d\Phi_k (2\pi)^4 \delta^4 \left( p_B - p_X - p_\ell - p_\nu - \sum k \right) \left| \sum_{n_V=0}^{\infty} \mathcal{M}_{n_R}^{n_V + \frac{1}{2}n_R} \right|^2 \quad (2.25)$$

can be rewritten as

$$\Gamma = \frac{1}{2M} \sum_{n_R=0}^{\infty} \frac{1}{n_R!} \int d\Phi_{p_f} d\Phi'_k (2\pi)^4 \delta^4 \left( p_B - p_X - p_\ell - p_\nu - \sum k \right) \times e^{Y(\Omega)} \prod_{i=1}^{n_R} \tilde{S}(k_i) \Theta(k_i, \Omega) \left( \tilde{\beta}_0^0 + \tilde{\beta}_0^1 + \sum_{i=1}^{n_R} \frac{\tilde{\beta}_1^1(k_i)}{\tilde{S}(k_i)} + \mathcal{O}(\alpha^2) \right) \quad (2.26)$$

by separating the universal spin-independent infrared divergent terms from the virtual and real emission amplitudes.  $d\Phi_{p_f}$  and  $d\Phi_k$  are the leading order and (multiple) extra emission phase space elements, while  $n_R$  and  $n_V$  count the additional real and virtual photons present in each amplitude. Therefore, using the same convention as before the sub- and superscripts of the (squared) matrix elements  $\mathcal{M}$ ,  $M$  and  $\tilde{\beta}$  denote their real emission photon multiplicity and their order of  $\alpha$  in the perturbative expansion relative to the leading order.

The separation of infrared divergences proceeds by splitting

$$\mathcal{M}_0^1 = \alpha B \mathcal{M}_0^0 + M_0^1, \quad (2.27)$$

$$\frac{1}{2(2\pi)^3} |M_1^{\frac{1}{2}}|^2 = \tilde{S}(k) |M_0^0|^2 + \tilde{\beta}_1^1(k), \quad (2.28)$$

wherein  $M_0^1$  and  $\tilde{\beta}_1^1(k)$  are free of any infrared singularities due to virtual or real photon emissions. This separation can be continued iteratively, leading to

$$\left| \sum_{n_V=0}^{\infty} \mathcal{M}_{n_R}^{n_V + \frac{1}{2}n_R} \right|^2 = \exp(2\alpha B) \left| \sum_{n_V=0}^{\infty} M_{n_R}^{n_V + \frac{1}{2}n_R} \right|^2. \quad (2.29)$$

and

$$\begin{aligned}
& \left( \frac{1}{2(2\pi)^3} \right)^{n_R} \left| \sum_{n_V=0}^{\infty} M_{n_R}^{n_V + \frac{1}{2}n_R} \right|^2 \\
&= \tilde{\beta}_0 \prod_{i=1}^{n_R} \left[ \tilde{S}(k_i) \right] + \sum_{i=1}^{n_R} \left[ \frac{\tilde{\beta}_1(k_i)}{\tilde{S}(k_i)} \right] \prod_{j=1}^{n_R} \left[ \tilde{S}(k_j) \right] + \sum_{\substack{i,j=1 \\ i \neq j}}^{n_R} \left[ \frac{\tilde{\beta}_2(k_i, k_j)}{\tilde{S}(k_i)\tilde{S}(k_j)} \right] \prod_{l=1}^{n_R} \left[ \tilde{S}(k_l) \right] + \dots \\
&+ \sum_{i=1}^{n_R} \left[ \tilde{\beta}_{n_R-1}(k_1, \dots, k_{i-1}, k_{i+1}, \dots, k_{n_R}) \tilde{S}(k_i) \right] + \tilde{\beta}_{n_R}(k_1, \dots, k_{n_R}), \tag{2.30}
\end{aligned}$$

with  $\tilde{\beta}_{n_R} = \sum_{n_V=0}^{\infty} \tilde{\beta}_{n_R}^{n_V+n_R}$ . Note that for a given phase space configuration  $\{p_1, \dots, p_n, k_1, \dots, k_{n_R}\}$  the infrared subtracted squared matrix elements  $\tilde{\beta}_1(k_i)$  involve a projection onto the single emission subspace  $\{\mathcal{P}p_1, \dots, \mathcal{P}p_n, \mathcal{P}k_i\}$ . Of course, momentum conservation holds for each projected subset. Thus, for every radiated photon the  $\tilde{\beta}_1(k_i)$  are evaluated as if this photon was the only one in the event. Hence, truncating the perturbative series in the  $\tilde{\beta}_{n_R}$  at the next-to-leading order leaves every single photon emission correct at  $\mathcal{O}(\alpha)$ .

Exponentiating the integral of the eikonal  $\tilde{S}(k)$  upon insertion of the identity of eq. (2.30) over the unresolved phase space  $\Omega$ , containing the infrared singularity gives rise to the Yennie-Frautschi-Suura form factor

$$Y(\Omega) = 2\alpha(B + \tilde{B}(\Omega)) \quad \text{with} \quad 2\alpha\tilde{B}(\Omega) = \int_{\Omega} \frac{d^3k}{k} \tilde{S}(k) \tag{2.31}$$

and the residual perturbative series of the infrared-subtracted squared amplitudes  $\tilde{\beta}_{n_R}^{n_V+n_R}$  in eq. (2.26). Hence, photon emissions contained in the unresolved soft region  $\Omega$  are assumed to have a negligible effect on differential distributions, but are included in the overall normalisation. Furthermore,  $Y(\Omega)$  is UV-finite and, thus, does not interfere with renormalisation of the  $\tilde{\beta}_{n_R}^{n_V+n_R}$ .

### 3. Methods & Implementations

In this section a short overview over the generators used in this study and their underlying principles is given.

#### 3.1. BLOR

BLOR [18] is a fixed order Monte Carlo Event generator specialised on QED corrections in semileptonic  $B$  meson decays. It separately generates decays for the born ( $1 \rightarrow 3$ ) and real emission ( $1 \rightarrow 4$ ) phase space events according to their individual cross sections

$$\begin{aligned}
d\Gamma_{1 \rightarrow 3} &= d\Gamma_0^0 + d\Gamma_0^1 \\
d\Gamma_{1 \rightarrow 4} &= d\Gamma_1^1. \tag{3.1}
\end{aligned}$$

The infrared divergences present in  $d\Gamma_0^1$  and  $d\Gamma_1^1$  are regulated introducing a small but finite photon mass  $\lambda$  set to  $10^{-7}\text{GeV}$ . The expressions of Sec. 2.2 are altered accordingly.

#### 3.2. SHERPA/PHOTONS++

The SHERPA Monte Carlo [19] is a complete event generation frame work for high energy physics processes. Although its traditional strengths lie in the perturbative aspects of lepton and hadron

colliders it also encompasses several modules for all non-perturbative aspects. In this work the hadron decay module HADRONS++ [33] and the universal higher order QED correction tool PHOTONS++ [20] are used.

HADRONS++ generates the leading order decay events according to the respective form factor parametrisations of the involved hadronic and leptonic currents. PHOTONS++ then rewrites the differential all orders inclusive decay width of eq. (2.26) as

$$\Gamma = \Gamma_0 \sum_{n_\gamma} \frac{1}{n_\gamma!} \int d\Phi_k J_P(k) e^{Y(\Omega)} \prod_{i=1}^{n_\gamma} [\tilde{S}(k_i) \Theta(k_i, \Omega)] \left( 1 + \frac{\tilde{\beta}_0^1}{\tilde{\beta}_0^0} + \sum_{i=1}^{n_R} \frac{\tilde{\beta}_1^1(k_i)}{\tilde{\beta}_0^0 \cdot \tilde{S}(k_i)} + \mathcal{O}(\alpha^2) \right), \quad (3.2)$$

cf. [20]. Hence, the leading order input is corrected both for soft photon effects to all orders and hard photon emission to an arbitrary order.  $J_P \leq 1$  represents the various Jacobians occurring when factoring out the leading order term. The perturbative series in the infrared-subtracted squared matrix elements includes only terms up to  $\mathcal{O}(\alpha)$  for this study. The NLO real emission squared amplitudes can alternatively be approximated using Catani-Seymour splitting function [34–36]

$$\tilde{\beta}_{1,\text{CS}}^1(k) = -\frac{\alpha}{4\pi^2} \sum_{i < j} Z_i Z_j \theta_i \theta_j (\bar{g}_{ij}(p_i, p_j, k) + \bar{g}_{ji}(p_j, p_i, k)) \tilde{\beta}_0^0, \quad (3.3)$$

where in  $i$  and  $j$  run over all particles in the process. The exact form of the  $\bar{g}_{ij}$  can be found in [20]. This approximation is also used if the exact real emission matrix element is not known. The infrared cut-off was set to  $10^{-6} \text{ GeV}$  in the rest frame of the charged dipole, i.e. the  $B^{+-} \ell^+$  or the  $X^{--} \ell^+$  system, respectively.

### 3.3. PHOTOS

The PHOTOS Monte Carlo [15] is an “after-burner” algorithm, which adds approximate bremsstrahlung corrections to leading order events produced by an external code. In this study it is taken as a reference for the differential distributions since it is widely in use. PHOTOS bases on the factorisation of the real emission matrix element in the collinear limit

$$|\mathcal{M}_1^{\frac{1}{2}}|^2 = \sum_i |\mathcal{M}_0^0|^2 \cdot f(p_i, k). \quad (3.4)$$

The radiation function  $f(p_i, k)$  is given to leading logarithmic accuracy. It incorporates the Altarelli-Parisi emission kernel for radiation off the particular final state particle. Its exact form is spin dependent and can be found in [15, 16]. In its exponentiated mode the number of photons follows a Poissonian distribution, while the individual photon’s kinematics are determined by applying above equation iteratively. To also recover the soft limit of real photon emission matrix elements an additional weight was introduced [37]

$$W_{\text{soft}} = \frac{\sum_{i=1}^{n_\gamma} \left| \sum_{j=1}^{n_C} Q_j \frac{p_j \cdot \varepsilon_i^*}{p_j \cdot k_i} \right|^2}{\sum_{i=1}^{n_\gamma} \sum_{j=1}^{n_C} Q_j^2 \left| \frac{p_j \cdot \varepsilon_i^*}{p_j \cdot k_i} \right|^2}, \quad (3.5)$$

wherein  $n_\gamma$  and  $n_C$  are the photon and the final state charged multiplicity of the process. To regularise the emission function in the soft limit an energy cut-off is imposed in the rest frame of the decaying particle. The collinear divergence is regularised by the emitter’s mass.

Initial state radiation is not accounted for as the mass of the decaying particle is the largest scale in the process and there are no associated collinear divergences or logarithmic enhancements. It could only be accounted for by supplementing PHOTOS with a matrix element correction. In case of heavy initial states eq. (3.5) still approximately recovers the soft limit.

In this analysis PHOTOS version 2.13 has been used in its exponentiated mode, including the soft interference terms. The infrared cut-off was set to  $10^{-7}m_{B^{0,+}}$ , respectively. BLOR supplemented the leading order decay events.

## 4. Results

Parameter	Value	Parameter	Value
$m_{\Upsilon(4S)}$	10.5794 GeV	$m_e$	0.0005109989 GeV
$\Gamma_{\Upsilon(4S)}$	20.5 MeV	$m_\mu$	0.10565837 GeV
$m_{B^0}$	5.27950 GeV	$m_{\nu_e}$	0
$m_{B^+}$	5.27913 GeV	$m_{\nu_\mu}$	0
$m_{D^0}$	1.86950 GeV	$m_W$	80.419 GeV
$m_{D^-}$	1.86484 GeV	$\alpha$	1/137.035999
$m_{D_0^{*0}}$	2.403 GeV	$G_F$	$1.16637 \cdot 10^{-5} \text{ GeV}^{-2}$
$m_{D_0^-}$	2.352 GeV		
$m_{\pi^0}$	0.134976 GeV		
$m_{\pi^-}$	0.13957 GeV		

**Tab. 1** Parameters used for all inclusive and differential decay rate calculations. All particle widths, except the  $\Upsilon(4S)$  width, are considered negligible.

In this section the results of the inclusion of the complete next-to-leading order corrections, both real and virtual short and long distance contributions, are reviewed for different decay channels with different form factor parametrisations of the hadronic current. First, results for the next-to-leading order inclusive decay rates and their effects on the extraction of  $|V_{xb}|$  from decay measurements will be shown in Sec. 4.1. Then, in Sec. 4.2 the effects on differential distributions and spectra are investigated and compared against the standard tool used in many experimental analyses, PHOTOS. The parameters used are detailed in Tab. 1.

### 4.1. Next-to-leading order corrections to decay rates

One key prediction of this publication is the process specific correction factor for higher order electroweak effects. These higher order corrections enter measurements of the CKM mixing angles  $V_{xb}$  via

$$\Gamma_{\text{measured}} = \eta_{\text{QCD}}^2 \eta_{\text{EW}}^2 |V_{xb}|^2 \tilde{\Gamma}_{\text{LO}}, \quad (4.1)$$

and, thus,

$$|V_{xb}| = \frac{1}{\eta_{\text{EW}}} \cdot \sqrt{\frac{\Gamma_{\text{measured}}}{\eta_{\text{QCD}}^2 \tilde{\Gamma}_{\text{LO}}}}. \quad (4.2)$$

$\tilde{\Gamma}_{\text{LO}}$  is the leading order phenomenological decay rate stripped of the CKM mixing angle.  $\eta_{\text{QCD}}$  and  $\eta_{\text{EW}}$  incorporate the higher order QCD and electroweak corrections. Both contributions

	$\eta_{\text{EW}}^2$	$1/\eta_{\text{EW}}$
$B^0 \rightarrow D^- e^+ \nu_e (\gamma)$	$1.0222(1 \pm 2 \pm 17 \pm 1)$	$0.9891(1 \pm 1 \pm 4 \pm 1)$
$B^0 \rightarrow D^- \mu^+ \nu_\mu (\gamma)$	$1.0222(1 \pm 2 \pm 17 \pm 1)$	$0.9891(1 \pm 1 \pm 4 \pm 1)$
$B^+ \rightarrow \bar{D}^0 e^+ \nu_e (\gamma)$	$1.0146(1 \pm 1 \pm 39 \pm 16)$	$0.9928(1 \pm 1 \pm 10 \pm 4)$
$B^+ \rightarrow \bar{D}^0 \mu^+ \nu_\mu (\gamma)$	$1.0147(1 \pm 1 \pm 39 \pm 16)$	$0.9927(1 \pm 1 \pm 10 \pm 4)$
$B^0 \rightarrow \pi^- e^+ \nu_e (\gamma)$	$1.0555(1 \pm 4 \pm 148 \pm 48)$	$0.9734(1 \pm 1 \pm 33 \pm 10)$
$B^0 \rightarrow \pi^- \mu^+ \nu_\mu (\gamma)$	$1.0545(1 \pm 4 \pm 136 \pm 48)$	$0.9738(1 \pm 1 \pm 31 \pm 11)$
$B^+ \rightarrow \pi^0 e^+ \nu_e (\gamma)$	$1.0411(1 \pm 3 \pm 100)$	$0.9801(1 \pm 1 \pm 23)$
$B^+ \rightarrow \pi^0 \mu^+ \nu_\mu (\gamma)$	$1.0401(1 \pm 3 \pm 89)$	$0.9805(1 \pm 1 \pm 21)$
$B^0 \rightarrow D_0^{*-} e^+ \nu_e (\gamma)$	$1.0224(1 \pm 2 \pm 10)$	$0.9890(1 \pm 1 \pm 2)$
$B^0 \rightarrow D_0^{*-} \mu^+ \nu_\mu (\gamma)$	$1.0226(1 \pm 2 \pm 10)$	$0.9889(1 \pm 1 \pm 2)$
$B^+ \rightarrow \bar{D}_0^{*0} e^+ \nu_e (\gamma)$	$1.0142(1 \pm 1 \pm 35)$	$0.9930(1 \pm 1 \pm 8)$
$B^+ \rightarrow \bar{D}_0^{*0} \mu^+ \nu_\mu (\gamma)$	$1.0144(1 \pm 1 \pm 35)$	$0.9929(1 \pm 1 \pm 8)$

**Tab. 2** Predictions for  $\eta_{\text{EW}} = \sqrt{1 + \delta_{\text{sd}} + \delta_{\text{ld}}}$  for the summed next-to-leading corrections are listed. The uncertainties in the parentheses are the sum of numerical, next-to-next-to-leading order, matching and missing structure dependent contributions. For  $B^+ \rightarrow \pi^0 \ell \nu (\gamma)$  and  $B^{0,+} \rightarrow D_0^{*-0} \ell \nu (\gamma)$  decays no predictions for structure dependent contributions are known.

factorise at the NLO level. The electroweak correction factor is determined in this study at NLO accuracy in the QED-improved phenomenological long-distance description of the hadronic decay and at leading logarithmic accuracy in the underlying short-distance partonic decay in the Standard Model. While the leading logarithm of the short-distance correction depends only on the matching scale  $\Lambda$  of both descriptions and is, thus, independent of the actual decay properties, the long-distance corrections, in contrast, are sensitive to exactly these specifics. The resulting correction factors,

$$\eta_{\text{EW}}^2 = 1 + \delta_{\text{sd}} + \delta_{\text{ld}} = 1 + \frac{\Gamma_0^1 + \Gamma_1^1}{\Gamma_0^0} + \mathcal{O}(\alpha^2) \quad (4.3)$$

are a central outcome of this study. They are presented in Tab. 2 for the different semileptonic decay channels of charged and neutral  $B$  mesons into (pseudo)scalar mesons. As is evident, the long-distance QED corrections break the strong isospin symmetry. This originates in the different masses of the charged mesons in the strong isospin rotated decays. These masses both determine the amount of radiation from the meson line and enter the loop integrals. For the same reasons the corrections for pions are larger than for  $D$  mesons. On the other hand, the difference in the size of the correction between the two leptonic channels of each decay mode is only very small since both masses are insignificant compared to the hadronic mass scales.

The total uncertainty  $\sigma_{\text{total}}$  of the summed long- and short-distance correction is given by

$$\sigma_{\text{total}}^2 = \sigma_{\text{numerical}}^2 + \sigma_{\text{nnlo}}^2 + \sigma_{\Lambda}^2 + \sigma_{\text{SD}}^2. \quad (4.4)$$

The leading uncertainty originates from the matching of the short- and long-distance results. Here, the mismatch of both theories, the Standard Model for the short-distance corrections and the QED-enhanced effective theory for the long-distance corrections, at the scale  $\Lambda$ , as discussed in Sec. 2.2.1, is the main source. These matching uncertainties are estimated choosing  $\Lambda$  of the scale of the final state meson's mass as a central value for  $\Lambda$  and then taking the difference to the result when using the scale  $2\Lambda$ . Note that half the charged final state meson's mass is not a sensible choice for the matching scale since in this case a considerable fraction of the



	$\eta_{\text{EW}}^2$	$1/\eta_{\text{EW}}$
$B^0 \rightarrow D^- \ell \nu$	1.0222(17)	0.9891(4)
$B^+ \rightarrow D^0 \ell \nu$	1.0146(43)	0.9928(10)
$B \rightarrow D \ell \nu$	1.0186(29)	0.9909(7)
	$\eta_{\text{EW}}^2$	$1/\eta_{\text{EW}}$
$B^0 \rightarrow \pi^- \ell \nu$	1.0550(150)	0.9736(34)

**Tab. 3** Averaged integration results for  $\eta_{\text{EW}}^2 = 1 + \delta_{\text{sd}} + \delta_{\text{ld}}$  and  $1/\eta_{\text{EW}}$ : The uncertainties in the parentheses are the sum of numerical, next-to-next-to-leading order, matching and missing structure dependent contributions.

Measurement	$\mathcal{G}(1)  V_{\text{cb}}  \times 10^{-3}$ with sd corrections only	$\mathcal{G}(1)  V_{\text{cb}}  \times 10^{-3}$ with sd and ld corrections
BABAR tagged [38]	42.30(2.36)	42.21(2.34)
Measurement	$ V_{\text{ub}}  \times 10^{-3}$ with no corrections	$ V_{\text{ub}}  \times 10^{-3}$ with sd and ld corrections
BABAR untagged [39]	3.60( $^{+0.62}_{-0.42}$ )	3.50( $^{+0.61}_{-0.42}$ )

**Tab. 4** The impact of long-distance corrections on the correction factor  $\eta_{\text{EW}}$  is shown. Both measurements estimate real next-to-leading order corrections via PHOTOS and, thus, use phase-space cuts and variables that provide a reduced sensitivity on the modeling of final state radiation.  $\mathcal{G}(1)$  is the normalisation of the heavy quark form factor. Note that  $|V_{\text{ub}}|$  aimed analyses usually do not apply short-distance corrections and that the form factor prediction of [40] was used to extract  $|V_{\text{ub}}|$  from the measured  $B^0 \rightarrow \pi^- \ell^+ \nu_\ell$  partial branching fraction.

real radiation cross section would occur at scales greater than  $\Lambda$  and being described by the phenomenological model, thus ending up in the wrong picture.

Along these lines, also again referring to Sec. 2.2.1, the results for decays into pions should be considered with care: apart from the afore mentioned conceptual problems introduced by the large separation of both hadronic mass scales, large parts of the real emission phase space, described in the phenomenological model with a point-like pion, are actually able to resolve the pion, the charged and the neutral one. Thus, the model used in this study is not entirely accurate for such decays.

Further, the effect of additional real short-distance contributions is studied by comparing the pure inner-bremsstrahlung calculation with the real emission results of [31] and [28]. This, however, can only be done for and  $B \rightarrow D \ell \nu (\gamma)$  and  $B^0 \rightarrow \pi^- \ell^+ \nu (\gamma)$  decays. Such terms are unknown for the other decay modes. Consequently, no error can be associated with them. Finally, the electroweak next-to-next-to-leading order effects are estimated as  $\sigma_{\text{nnlo}} = \alpha (\delta_{\text{sd}} + \delta_{\text{ld}})$ . It is clear that the complete model dependence from our phenomenological treatment of the long-distance contributions cannot be grasped with the above error estimation.

Tab. 3 presents the same results for  $B \rightarrow D \ell \nu (\gamma)$  and  $B^0 \rightarrow \pi^- \ell^+ \nu (\gamma)$  averaged over the different lepton species and the isospin rotated decays. The isospin averaged result is corrected for the difference in the production rate of  $B^0$  and  $B^+$  mesons, i.e.

$$\delta_{\text{sd}} + \delta_{\text{ld}} = (\delta_{\text{sd}} + \delta_{\text{ld}}^+) f_{+-} + (\delta_{\text{sd}} + \delta_{\text{ld}}^0) f_{00}, \quad (4.5)$$

with  $\delta_{\text{ld}}^+$  and  $\delta_{\text{ld}}^0$  the isospin breaking contributions for charged and uncharged charmed decays

extracted from Tab. 2. The latter correction factor is the adequate choice to correct  $|V_{cb}|$  from measurements demanding isospin.

The impact of these correction factors on two selected measurements are listed in Tab. 4. Note that both measurements used PHOTOS to estimate the effect on radiative corrections. Applying the stated factors only corrects the overall normalisation, differences due to changes in kinematic distributions, see Sec. 4.2, result in another correction for the extracted values of  $|V_{cb}|$  and  $|V_{ub}|$  that cannot be estimated here. The correction for  $|V_{ub}|$  shown here is therefore an illustration only and should be used with care.

## 4.2. Next-to-leading order corrections to differential rates

In this section the results of both BLOR and SHERPA/PHOTONS++ are presented and compared against PHOTOS. The focus lies on the absolute value of the spatial momentum of the produced meson and the lepton, i.e.  $|\vec{p}_X|$  and  $|\vec{p}_\ell|$ . The chosen frame for these observables is the centre-of-momentum system of the electron and positron beam. Thus, the decaying  $B^0$  and  $B^+$  mesons already carry momentum corresponding to the  $\Upsilon(4S) \rightarrow B^0 \bar{B}^0$  and  $\Upsilon(4S) \rightarrow B^+ B^-$  decay kinematics. All quantities are shown as bare quantities, i.e. no recombination of photon and lepton/meson momenta was used. This is directly applicable if the charged particle momenta are extracted by measuring their curved tracks in a magnetic field or in photon-free calorimeters, as is the case in many BABAR and BELLE analyses.

The prediction of each generator is normed to its inclusive decay width and the ratio plots show the relative difference

$$\Delta_O = \frac{\frac{1}{\Gamma_{\text{tot},i}} \frac{d\Gamma_i}{dO} - \frac{1}{\Gamma_{\text{tot,ref}}} \frac{d\Gamma_{\text{ref}}}{dO}}{\frac{1}{\Gamma_{\text{tot},i}} \frac{d\Gamma_i}{dO} + \frac{1}{\Gamma_{\text{tot,ref}}} \frac{d\Gamma_{\text{ref}}}{dO}}$$

to the PHOTOS prediction for the given observable  $O$  in the given bin. Hence, the shortcomings of the approximations inherent in the standard tool currently used by most experiments are plainly visible. Further, due to the choice of normalisation, systematic errors, shown to be dominant in the previous section, are negligible here. Hence, the error bands shown are statistical errors only and are of comparable magnitude for all three generators predictions.

### 4.2.1. Decays $B \rightarrow D \ell \nu_\ell$

In Fig. 5 the predictions of all three generators for the decay  $B^0 \rightarrow D^- e^+ \nu_e$  using a form factor parametrisation from Heavy Quark Effective Theory, cf. App. A.1, are presented. For most of the phase space the agreement of the next-to-leading order shape is good. However, as can be seen in the absolute lepton momentum plot, SHERPA/PHOTONS++ predicts a slightly different shape close to  $|\vec{p}_\ell|, |\vec{p}_X| = 0$ . This limit cannot be measured directly in most experiments. Nonetheless, it influences the extrapolation to the full phase space, and thus determinations of total decay widths. In [41], for example, uncertainties related to such an extrapolation constituted up to 50% of the total experimental error. Further, the slight slope of the order of 1% exhibited in the prediction of SHERPA/PHOTONS++ for  $|\vec{p}_X|$  is also present in the  $|\vec{p}_\ell|$  spectrum. Both differences originate in the different modeling of radiative energy loss between the different programs, as shown in the following.

Fig. 6 displays the radiative energy loss, i.e. the sum of the energies of all photons radiated, in the rest frame of the decaying  $B^0$ . The predictions of the three different generators are shown in the left panel. For single photon emission in such a final state dipole there exists a kinematic limit on the photon's energy:  $E_\gamma^{\text{max}} = \frac{m_B}{2} \left( \frac{m_B}{m_X + m_\ell} - \frac{m_X + m_\ell}{m_B} \right)$  in the dipole's rest frame or  $E_\gamma^{\text{max}} =$

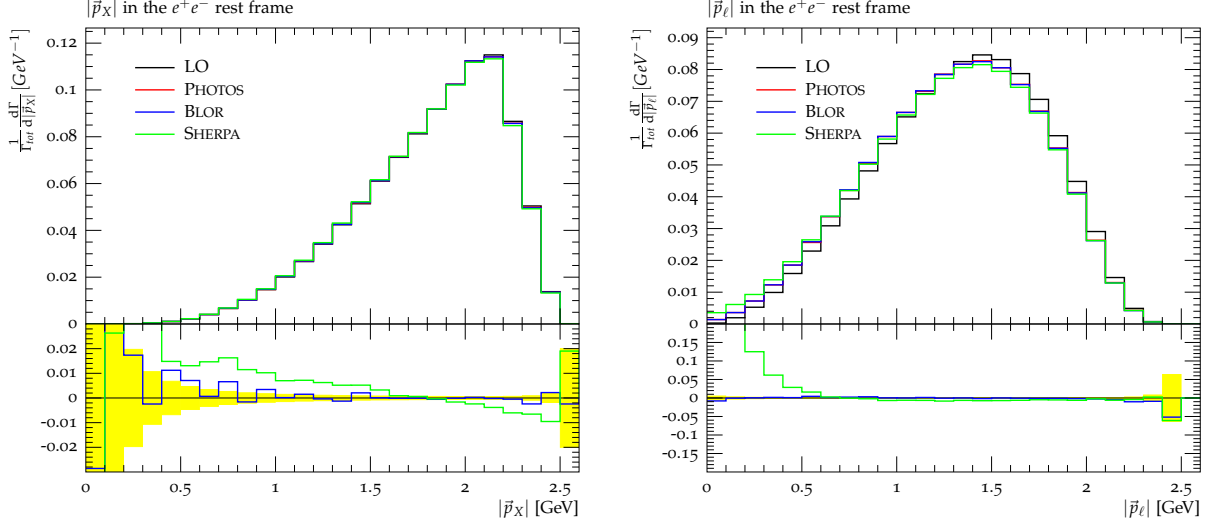


**Fig. 5** Lepton and Meson momentum spectrum in the  $e^+e^-$  rest frame in the decay  $B^0 \rightarrow D^- e^+ \nu_e$ . All spectra are normed to the total inclusive decay width predicted by the respective generator. The ratio plot gives the relative deviation, bin by bin, of the predicted shapes with PHOTOS as reference. The shaded yellow area gives the statistical uncertainty of the reference distribution.

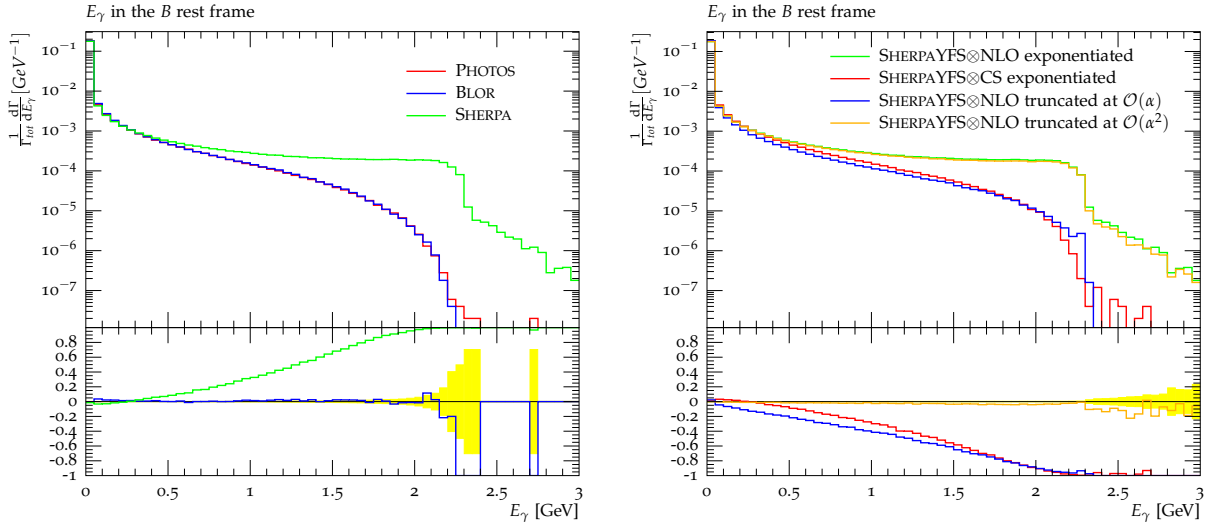


**Fig. 6** Total radiative energy loss, i.e. the sum of all photons radiated, in the decay  $B^0 \rightarrow D^- e^+ \nu_e$  in the  $B$  rest frame. All spectra are normed to the total inclusive decay width predicted by the respective generator. The left panel shows the predictions of all three generators and the PHOTOS prediction is taken as the reference in the ratio plot. The right panel shows the predictions of SHERPA/PHOTONS++ in its full YFS $\otimes$ NLO exponentiated mode (green), a mode where the exact NLO matrix element of the perturbative expansion is replaced by universal Catani-Seymour dipole splitting kernels (red) and two modes where the exact real emission matrix elements are used, but the expansion in the resolved emission region is truncated at  $\mathcal{O}(\alpha)$  (blue) and  $\mathcal{O}(\alpha^2)$  (orange), thus allowing at most one and two photons, respectively. Here, the full exponentiated SHERPA/PHOTONS++ prediction is taken as reference in the ratio plot.

2.3083 GeV in the  $B$  rest frame. This limit is clearly visible in Fig. 6. All events exceeding it, i.e. radiating more than  $E_\gamma^{\max}$ , must exhibit multi-photon radiation. Here (at least) two hard photons recoil against each other. Hence, this feature is present in both the SHERPA/PHOTONS++ and PHOTOS predictions, but not in the fixed order NLO prediction of BLOR. This tail is an  $\mathcal{O}(\alpha^2)$  effect in the hard radiation and can only be described approximatively here. In PHOTOS it is described by an iteration of the emission kernels while SHERPA/PHOTONS++ describes this part of the spectrum by the next-to-leading order hard emission amplitude  $\tilde{\beta}_1^{\dagger}$  summed over all projections onto the single emission subspaces, cf. Sec. 2.4 and 3.2.

On the other hand, multi-photon radiation also enhances the amount of radiation in the region  $E_\gamma < E_\gamma^{\max}$ , if the probability of two relatively hard photons is sufficiently large. As exemplified in Fig. 7, in  $B^0 \rightarrow D^- e^+ \nu_e$  double photon emission is relatively probable and, hence, leads to such an enhancement, whereas due to the much larger muon mass this feature is nearly absent in the decay to muons, Fig. 9. Of course, this enhancement of the radiative energy loss is an effect of  $\mathcal{O}(\alpha^2)$  and can therefore only be described approximatively here.

Of equal importance as multi-photon radiation is the presence of the exact real emission matrix element, as is also shown in the right panel of Figs. 6 and 9. Approximating the real emission matrix elements with Catani-Seymour splitting functions, reproducing the Altarelli-Parisi splitting functions used in PHOTOS in the (quasi-) collinear limit, leads to a mis-estimation of the radiative energy loss in the regime close to the kinematic boundary. It seems, however, that in the present cases collinearly approximated multi-photon emission mimics the exact fixed-order NLO behaviour reasonably well.

Close to the kinematic boundary on single photon emission,  $E_{\max}$ , the vertex emission diagrams become important, as do the corrections for  $t \neq t'$  (cf. App. B). These corrections have different sizes for the electron and muon channels due to their different masses and radiative properties. In principle, here also the structure-dependent corrections of Sec. 2.3 play a role. But, as is investigated in Sec. 4.3 they have negligible impact on the shape of the differential distributions. Thus, they can be safely neglected here.

Further, both SHERPA/PHOTONS++ and PHOTOS share a common soft limit, showing the compatibility of the inherent soft resummation of SHERPA/PHOTONS++ and the superimposed soft limit correction in PHOTOS. BLOR exhibits an (almost) constant off-set of a few percent owing to the lack of resummed contributions modeled in SHERPA/PHOTONS++ by virtue of the YFS form factor.

The lepton and meson spectra for  $B^0 \rightarrow D^- \mu^+ \nu_\mu$  are shown in Fig. 8. Figs. 10 and 11 show strong isospin rotated processes  $B^+ \rightarrow \bar{D}^0 e^+ \nu_e$  and  $B^+ \rightarrow \bar{D}^0 \mu^+ \nu_\mu$ , respectively. Thus, the radiating dipole is spanned between the initial state  $B^+$  and the lepton. Radiation off the initial state meson is suppressed by its much larger mass, as compared to the  $D^-$ . Thus, multi-photon emission is also strongly suppressed. In these cases SHERPA/PHOTONS++ predict slightly smaller radiative corrections in the electron decay channel than either PHOTOS or BLOR. The differences are of the order of five percent; note that the scale was enlarged in the reference plot to better highlight the differences. These, to the largest extent, root in differences in the modeling of emission off the initial state charged meson.

#### 4.2.2. Decays $B \rightarrow D_0^* \ell \nu_\ell$

The final state lepton and meson momentum spectra in the decays  $B^{0,+} \rightarrow \bar{D}_0^{*-,0} \ell^+ \nu_\ell$ , with  $\ell = e, \mu$ , are shown in Figs 12, 13, and 14, 15. The  $B \rightarrow D_0^*$  transition current is modeled using Leibovich-Ligeti-Stewart-Wise-parametrised form factors, cf. App. A.3. Except for differences in the form factor parametrisations due to the  $D_0^*$  meson being a scalar instead of a pseudo-

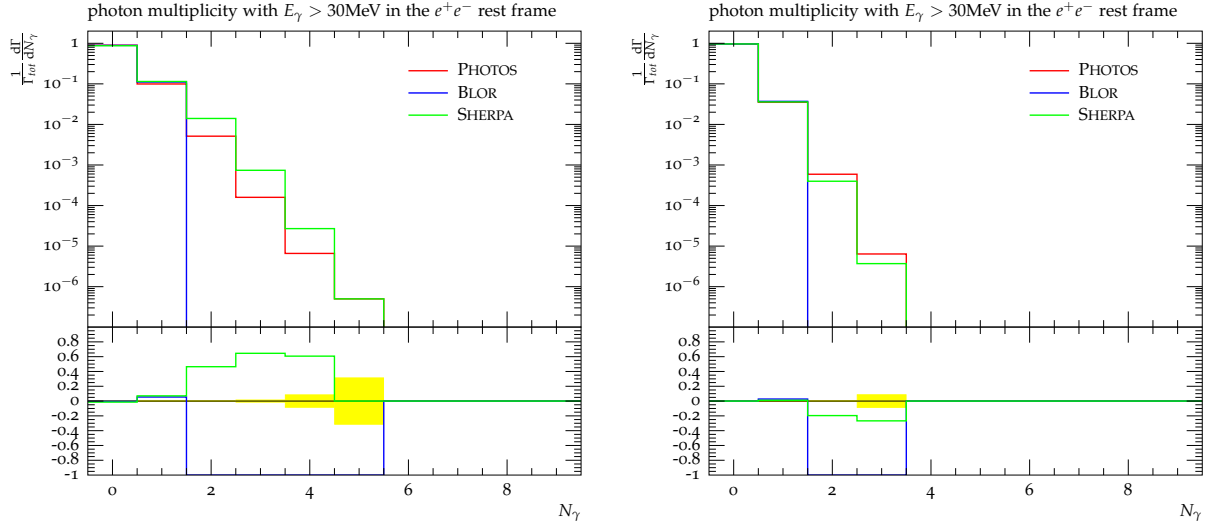


**Fig. 7** Multiplicities of photons with at least 30MeV in in the  $e^+e^-$  rest frame  $B^0 \rightarrow D^- e^+ \nu_e$  on the right hand side and  $B^0 \rightarrow D^- \mu^+ \nu_\mu$  on the left hand side. In the ratio plot PHOTOS was chosen as the reference.

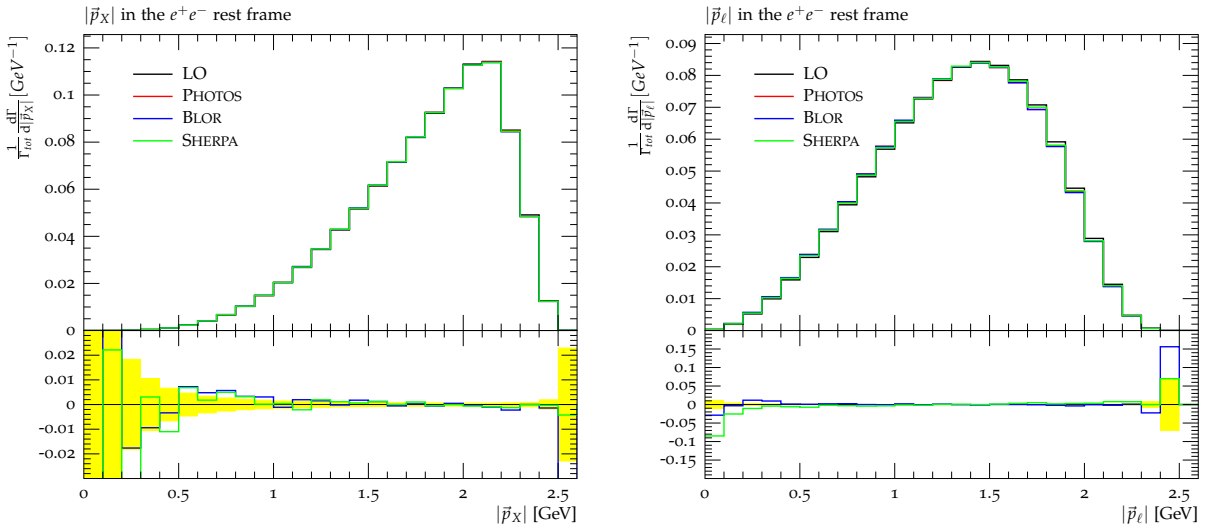


**Fig. 8** Lepton and Meson momentum spectrum in the  $e^+e^-$  rest frame in the decay  $B^0 \rightarrow D^- \mu^+ \nu_\mu$ . The PHOTOS prediction is taken as the reference in the ratio plot.

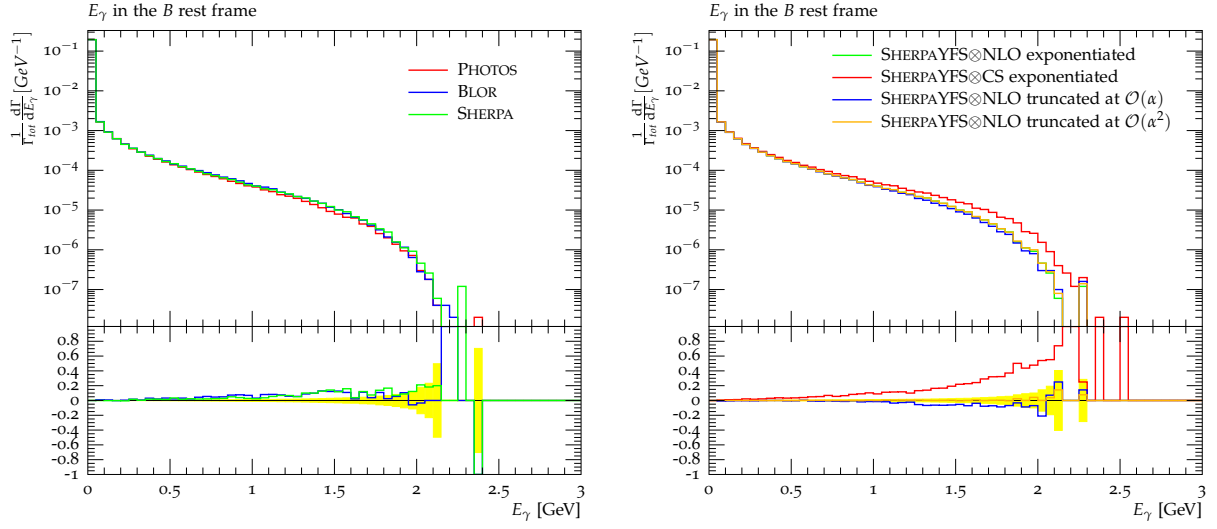


**Fig. 9** Total radiative energy loss, i.e. the sum of all photons radiated, in the decay  $B^0 \rightarrow D^- \mu^+ \nu_\mu$  in the  $B$  rest frame. The labels are identical to those in Fig. 6.

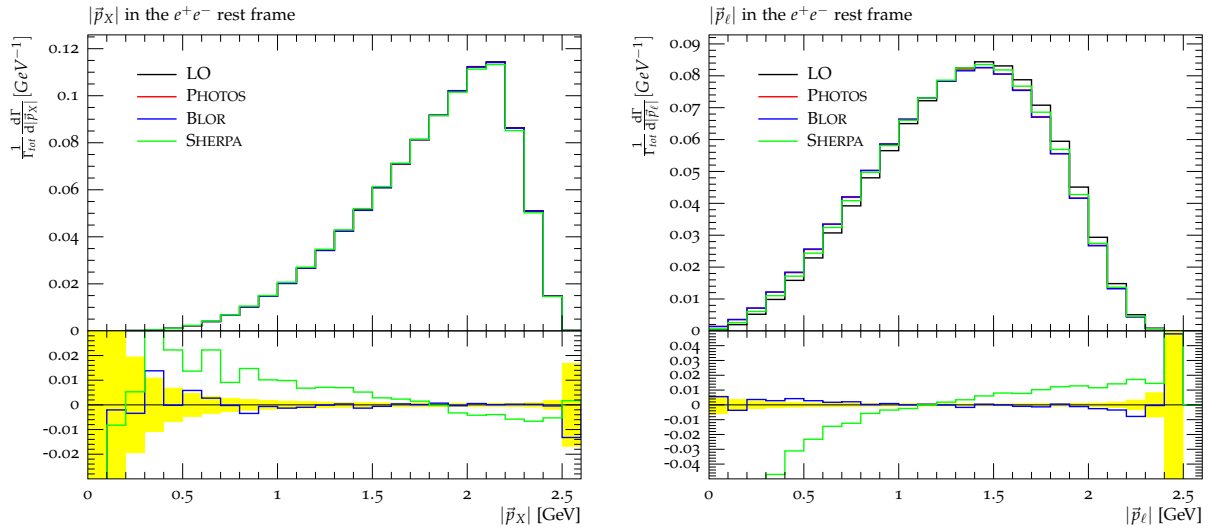


**Fig. 10** Lepton and Meson momentum spectrum in the  $e^+e^-$  rest frame in the decay  $B^+ \rightarrow \bar{D}^0 e^+ \nu_e$ . The PHOTOS prediction is taken as the reference in the ratio plot.

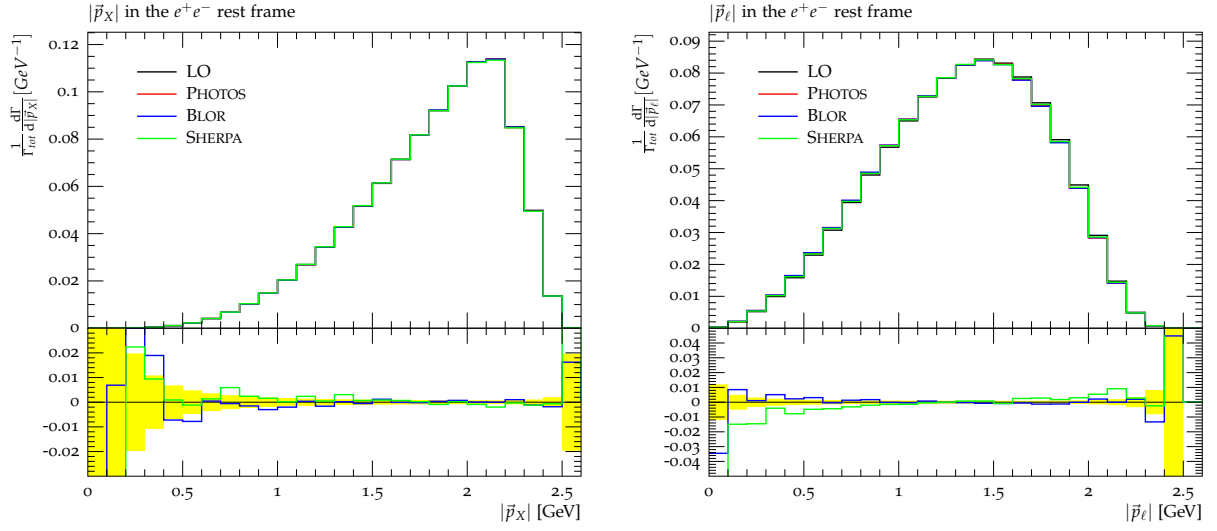


**Fig. 11** Lepton and Meson momentum spectrum in the  $e^+e^-$  rest frame in the decay  $B^+ \rightarrow \bar{D}^0 \mu^+ \nu_\mu$ . The PHOTOS prediction is taken as the reference in the ratio plot.

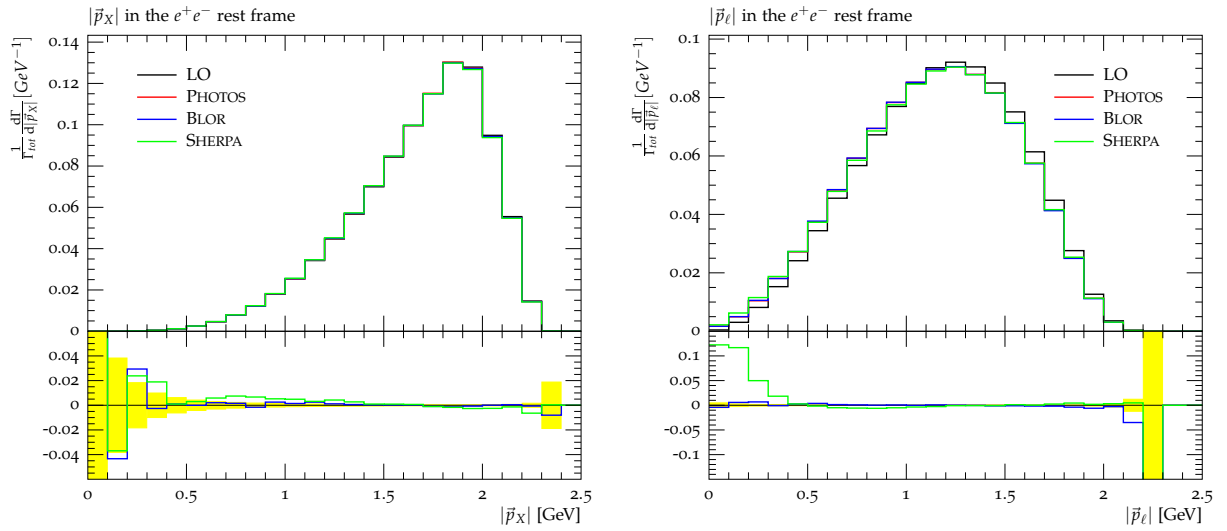


**Fig. 12** Lepton and Meson momentum spectrum in the  $e^+e^-$  rest frame in the decay  $B^0 \rightarrow D_0^{*-} e^+ \nu_e$ . The PHOTOS prediction is taken as the reference in the ratio plot.

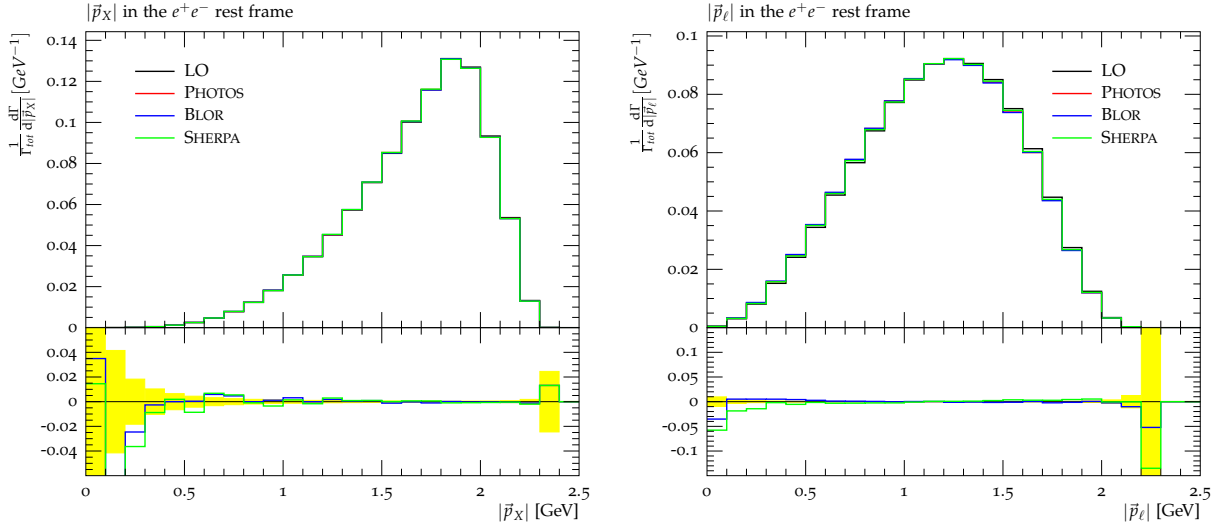


**Fig. 13** Lepton and Meson momentum spectrum in the  $e^+e^-$  rest frame in the decay  $B^0 \rightarrow D_0^{*-} \mu^+ \nu_\mu$ . The PHOTOS prediction is taken as the reference in the ratio plot.

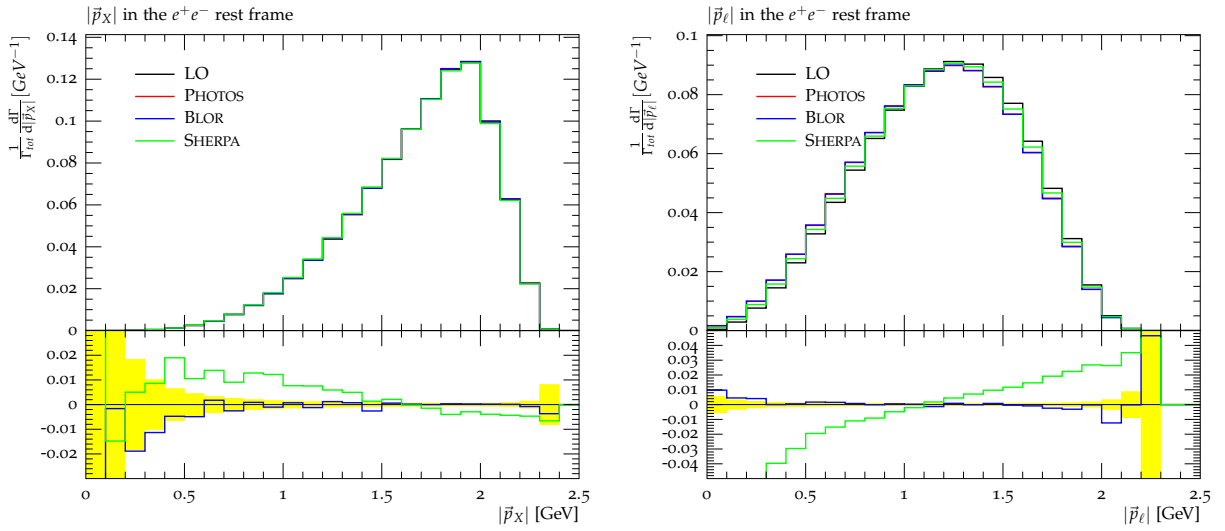


**Fig. 14** Lepton and Meson momentum spectrum in the  $e^+e^-$  rest frame in the decay  $B^+ \rightarrow \bar{D}_0^{*0} e^+ \nu_e$ . The PHOTOS prediction is taken as the reference in the ratio plot.



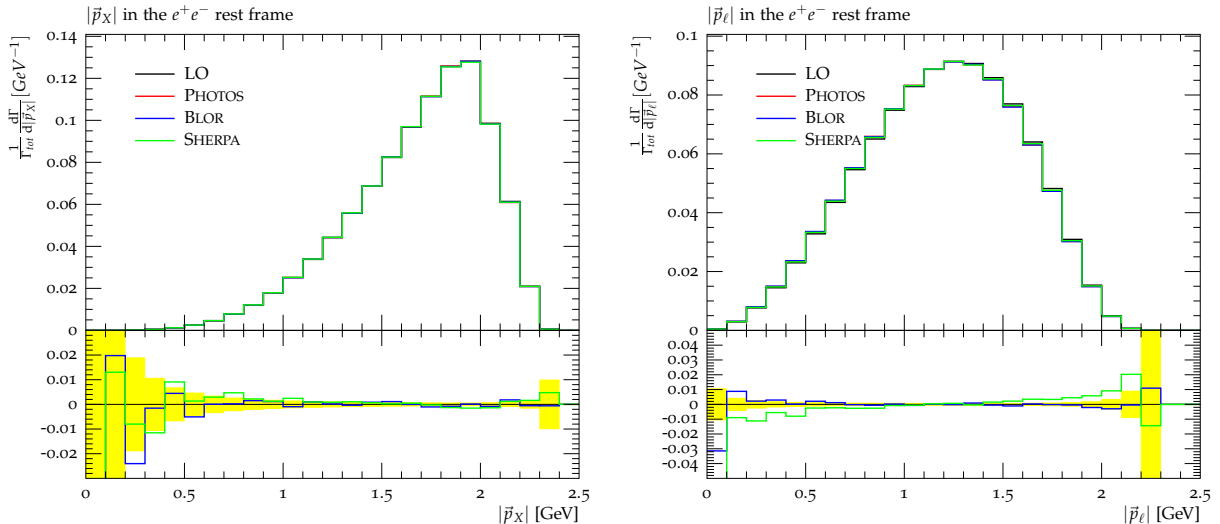


**Fig. 15** Lepton and Meson momentum spectrum in the  $e^+e^-$  rest frame in the decay  $B^+ \rightarrow \bar{D}_0^{*0} \mu^+ \nu_\mu$ . The PHOTOS prediction is taken as the reference in the ratio plot.

scalar and its higher mass, the effects of higher order corrections are comparable to the case of Sec. 4.2.1.

#### 4.2.3. Decays $B \rightarrow \pi \ell \nu_\ell$

Figs. 16, 17 and 18, 19 show the decay channels into charged and neutral pions. The  $B \rightarrow \pi$  transition current is modeled using the Ball-Zwicky form factor model described in App. A.2. Here, because of the comparably small mass of the charged pion effects due to IB corrections for  $t \neq t'$  become important. The structure-dependent contributions still have negligible impact on the differential distributions, as is shown in Sec. 4.3. Again, in the electron channel of the decay into a charged pion the correct treatment of hard multi-photon radiation, assuming they are sufficiently well described in the QED-enhanced phenomenological model, leads to comparably large deviations.

Nonetheless, it should be noted, as was also discussed earlier, that the matching procedure employed in this study runs into conceptual problems when applied to a  $B \rightarrow \pi$  transition due to large difference between the hadronic mass scale  $\Lambda = m_\pi$  and the maximal energy of an emitted photon,  $E_\gamma^{\max} = 2.6379\text{GeV}$  ( $B^0 \rightarrow \pi^- e^+ \nu_e$ ). Consequently, a considerable fraction of the real emission phase space wherein the photon is able to resolve the pion is described by the effective theory only. Thus, the results obtained here should be considered with caution. However, they still are an improvement over the leading logarithmic corrections employed in standard analyses.

### 4.3. Influence of explicit short-distance terms

In section the influence of explicitly calculated structure dependent terms, as introduced in Sec. 2.3, is investigated. The analysis is performed for the decay channel  $B^0 \rightarrow \pi^- e^+ \nu_e$  with the results of [31] and the decay channels  $B^{0,+} \rightarrow D^{-,0} e^+ \nu_e$  with the results of [28]. The same conclusions also apply to the muon channels.

For the charged pion channel, [31] employs a form factor model of the heavy-hadron chiral perturbation theory (HH $\chi$ pt) [42–45], valid in the region of  $E_\gamma > 1\text{GeV}$ . Despite the mismatch

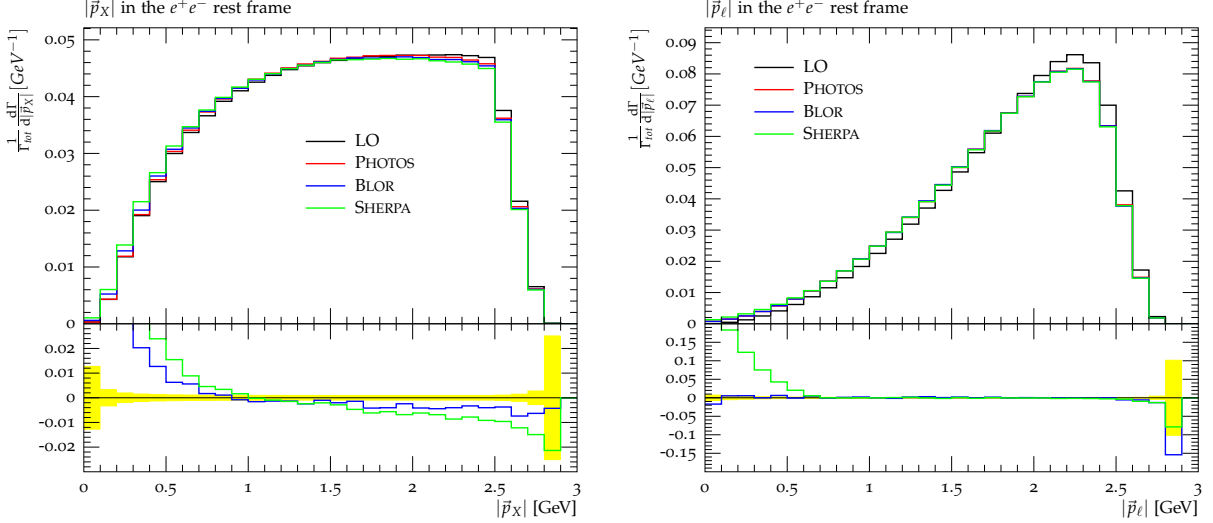


**Fig. 16** Lepton and Meson momentum spectrum in the  $e^+e^-$  rest frame in the decay  $B^0 \rightarrow \pi^- e^+ \nu_e$ . Both matrix-element-corrected multi-photon radiation and the IB terms for  $t \neq t'$  exhibit a strong influence here. The PHOTOS prediction is taken as the reference in the ratio plot.

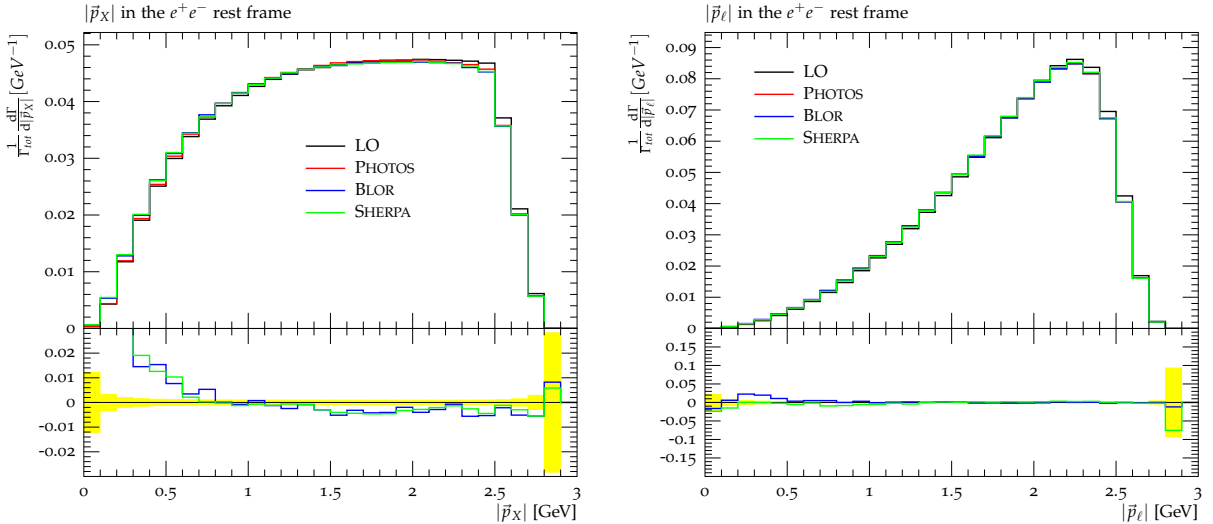


**Fig. 17** Lepton and Meson momentum spectrum in the  $e^+e^-$  rest frame in the decay  $B^0 \rightarrow \pi^- \mu^+ \nu_\mu$ . The IB terms for  $t \neq t'$  exhibit a strong influence here. The PHOTOS prediction is taken as the reference in the ratio plot.

	$\delta_{\text{sd}} + \delta_{\text{ld(IB)}}$	$\delta_{\text{sd}} + \delta_{\text{ld(IB+part.SD)}}$	$\sigma_{\text{SD}}$
$B^0 \rightarrow D^- \ell^+ \nu_\ell(\gamma)$	0.02223(6)	0.02225(7)	0.00002
$B^+ \rightarrow D^0 \ell^+ \nu_\ell(\gamma)$	0.01463(5)	0.01627(6)	0.00158

**Tab. 5** The effect of including the partial SD terms arising due to intermediate excited  $D^{*-}$  and  $D^{*0}$  mesons is shown. Because of the unknown size of the full SD contributions this single term, argued to be dominating, is used as an estimate on the systematic uncertainty  $\sigma_{\text{SD}}$  associated to the IB-only result of Sec. 4.1.

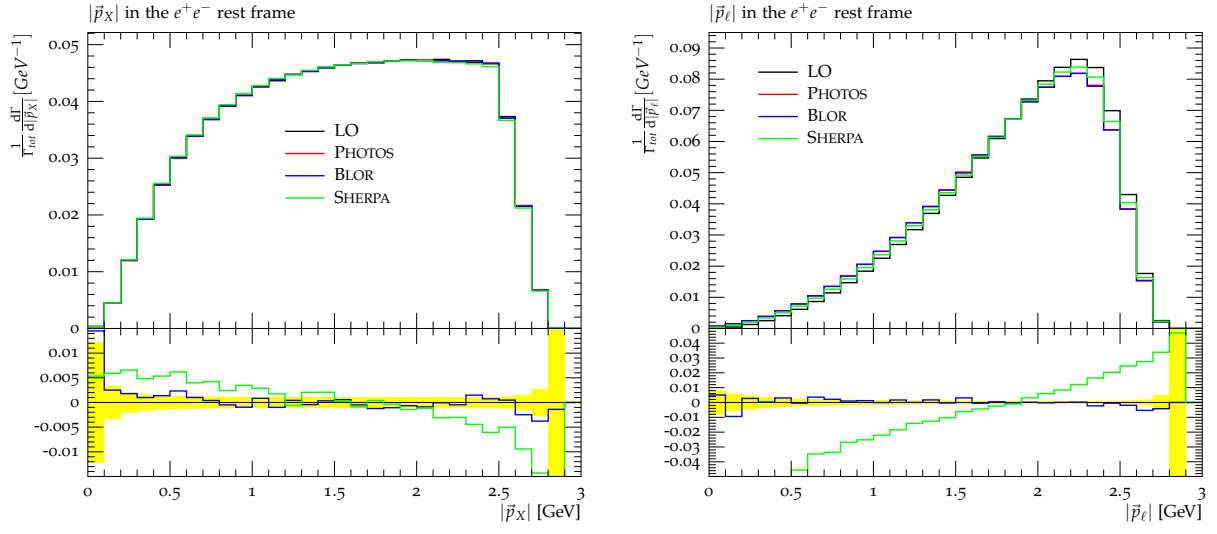


**Fig. 18** Lepton and Meson momentum spectrum in the  $e^+e^-$  rest frame in the decay  $B^+ \rightarrow \pi^0 e^+ \nu_e$ . The PHOTOS prediction is taken as the reference in the ratio plot.

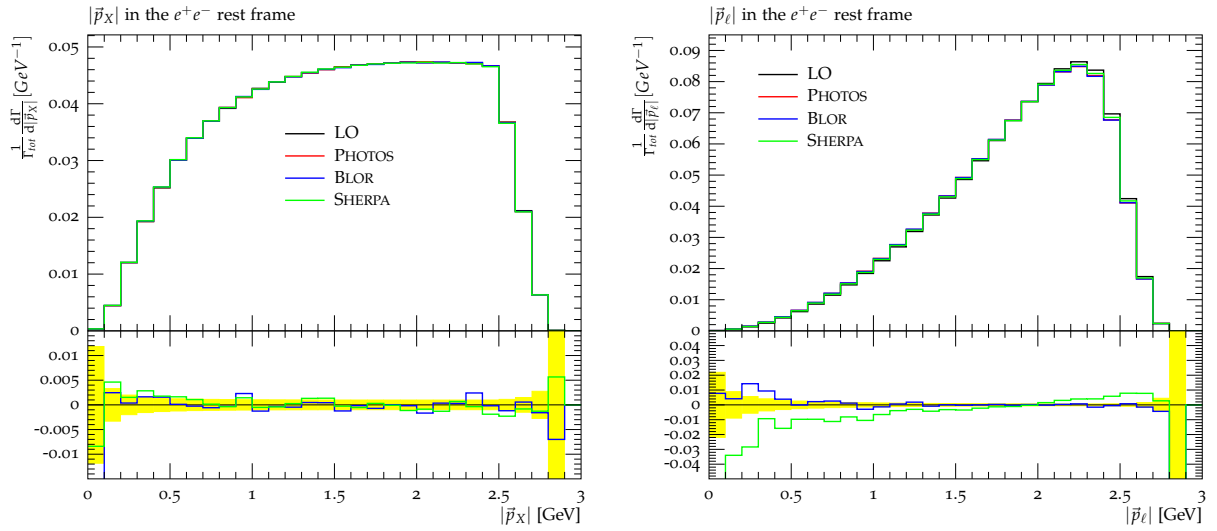


**Fig. 19** Lepton and Meson momentum spectrum in the  $e^+e^-$  rest frame in the decay  $B^+ \rightarrow \pi^0 \mu^+ \nu_\mu$ . The PHOTOS prediction is taken as the reference in the ratio plot.

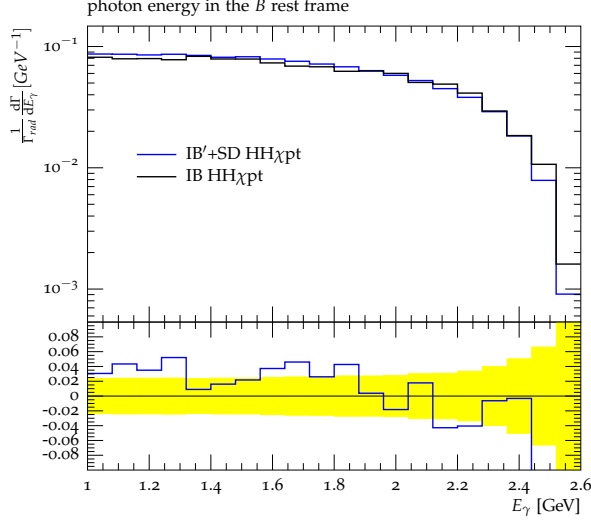


**Fig. 20** The photon energy spectrum in the decay  $B^0 \rightarrow \pi^- e^+ \nu_e \gamma$  ( $E_\gamma > 1\text{GeV}$ ) is shown. The complete IB+SD result of [31] (blue) is compared against the prediction of the IB terms only according to Sec. 2.3 (black) in the  $\text{HH}\chi_{\text{pt}}$  form factor model. In the ratio plot the latter is taken as the reference.

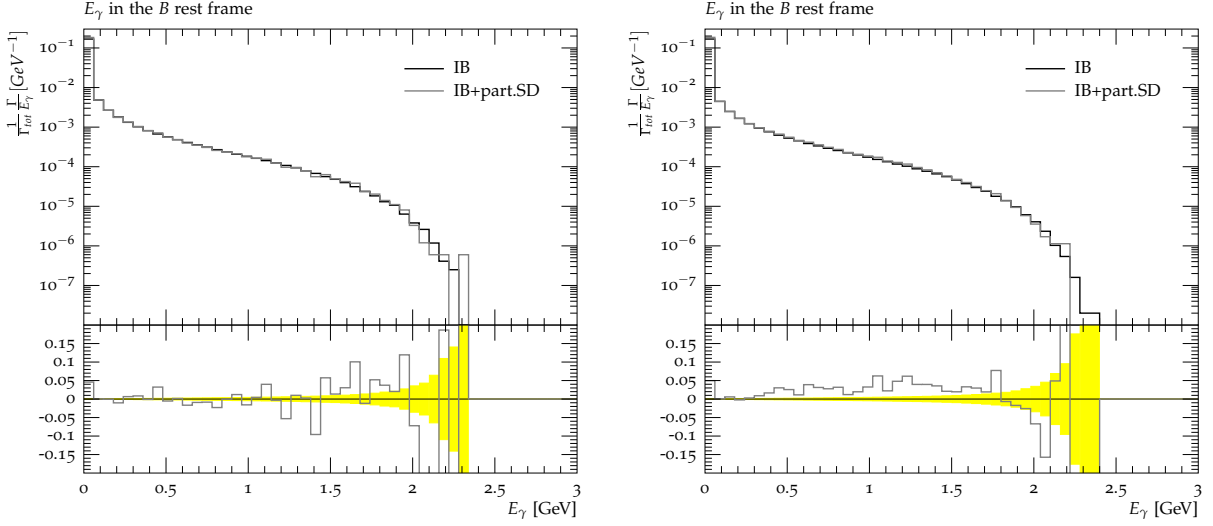


**Fig. 21** The photon energy spectra in the decays  $B^0 \rightarrow D^- e^+ \nu_e \gamma$  on the left and  $B^+ \rightarrow D^0 e^+ \nu_e \gamma$  on the right are shown. The result including partial SD terms arising due to intermediate excited mesons,  $D^{*-}$  and  $D^{*0}$  [28], and the associated coupling  $X^* \rightarrow X\gamma$  (grey) is compared against the prediction of the IB terms only according to Sec. 2.3 (black) in the HQET form factor model. In the ratio plot the latter is taken as the reference.

of the form factor model used in the present study the result depicted in Fig. 20 shows the structure-dependent contributions have little influence on the photon energy spectrum in this region. Due to their finiteness in the limit  $k \rightarrow 0$ , they are expected to behave similarly for  $E_\gamma < 1\text{GeV}$ . For the Ball-Zwicky form factor model used in this study, cf. App. A.2, the IB and SD correction are expected to behave similarly.

In the  $D$  meson channels, [28] uses lattice results for the trilinear couplings of an excited  $D^*$  meson to a photon and its ground state:  $g_{D^{*+}D^+\gamma} = -0.1(7)$  and  $g_{D^{*0}D^0\gamma} = 2.7(1.2)$ . The effects manifest themselves as corrections to the total decay widths and are summarized in Tab. 5: they prove minor in the case of  $D^-$ , and sizable in the case of  $D^0$ . The case is similar for the radiative spectra: a slight change in the shape of the radiative energy loss for the  $D^0$  channel on the scale of less than 5%, while no such change occurs in the  $D^-$  channel. These particular SD corrections, however, only form a single term in one class of SD correction. Note that higher order charm resonances, i.e. through  $D^{**}D\gamma$  processes, do not contribute to real corrections at NLO of the studied decay modes because of angular momentum and spin conservation. Therefore, the lowest order are believed to be one of the dominant terms, they are taken as an estimate for the error associated to neglecting all SD contributions.

Note, that the samples containing (partial) SD terms have larger statistical uncertainties.

## 5. Conclusions

In this paper, electroweak correction to semileptonic  $B$  decays were studied. A long-distance calculation in the QED improved effective Lagrangian was matched to the partonic short-distance result of [8] for (pseudo)scalar final state mesons. Structure dependent terms, e.g. due to non-local photon-charged meson interactions, intermediate resonant meson propagators or modifications to the effective weak meson decay due to off-shell currents, were not taken into account for the computed central values. This was done because they are only known for a very limited set of processes, and there usually only partially.

The results achieved with this method, detailed in Sec. 4, give more reliable predictions for total and differential decay rates, accompanied by quantifiable errors. The improved predictions of the total decay rate were applied on two selected measurements of  $V_{cb}$  [38] and  $V_{ub}$  [39] resulting in small corrections to their respective central values. These exemplifications, however, are a mere reweighting of their stated results and correction factors. To fully assess the impact of the corrections to the leading order decay presented in this paper the form factors of the phenomenological models will have to be refitted with the results presented in Sec. 4.2. Here, special attention is again drawn to the large deviations near the endpoints of the kinematic distributions arising when both fixed next-to-leading order and resummed leading-logarithmic calculations are combined. Finally, the parts of the analyses relying on Monte Carlo estimates of the radiation pattern need to be corrected for the improved description presented in this publication.

It should again be emphasised that the results presented for the decay of a  $B$  meson into a pion should be considered with care. The prescription of matching long- and short-distance corrections runs into conceptual problems for this particular process. This is due to the large hierarchy of the scales of the pion mass (the scale where a photon is able to resolve a pion) and the maximally allowed photon energy ( $E_\gamma^{\text{max}} \sim 2.5\text{GeV}$ , cf. Sec. 4.2.3). Consequently, the prediction for the total decay rate may receive significant corrections when a more elaborate matching scheme is used. Nonetheless, the differential distributions are unaffected.

Similarly, structure-dependent contributions, where known, have been shown to have negligible

influence on the differential distributions while their impact on the total decay rates can be sizeable. Despite this fact, these structure-dependent contributions were not included in the predictions of the central values of the total decay rates, but only have been used to estimate their potential error. This treatment is justified since in all cases considered here they are only known partially.

## Acknowledgements

The authors would like to thank Heiko Lacker, Dominik Stöckinger, and Sébastien Descotes-Genon for useful discussions. MS thanks Frank Siegert for help in introducing new form factor models into SHERPA/HADRON+++. The work of MS was supported by the DFG Graduate College 1504 and the MCnet Marie Curie Research Training Network (contract number MRTN-CT-2006-035606).

All histograms were plotted using tools from Rivet [46].

## A. Form factor models of exclusive semileptonic $B$ meson decays reviewed.

### A.1. Form factors for $B \rightarrow D \ell \nu$

Parameter	Value
$\mathcal{G}(1)$	0.98
$\rho_D^2$	1.19

**Tab. 6** Parameter values used for the transition current  $\langle D|V^\mu|B \rangle$  taken from Heavy Quark Effective Theory.

The vector current describing the semileptonic  $B \rightarrow D \ell \nu$  decay is given by

$$\langle D|V^\mu|B \rangle = \sqrt{m_B m_D} (h_+(w)(v_B + v_D)^\mu + h_-(w)(v_B - v_D)^\mu), \quad (\text{A.1})$$

with the heavy quark form factors  $h_\pm$  parametrised [47]

$$h_+(w) = \mathcal{G}(1) \times [1 - 8\rho_D^2 z + (51\rho_D^2 - 10)z^2 - (252\rho_D^2 - 84)z^3], \quad (\text{A.2})$$

$$h_-(w) = 0. \quad (\text{A.3})$$

It is  $z = \frac{\sqrt{w+1}-\sqrt{2}}{\sqrt{w+1}+\sqrt{2}}$  with  $w = \frac{m_B^2 + m_D^2 - t}{2m_B m_D}$ ,  $\rho_D^2$  the form factor slope, and  $\mathcal{G}(1)$  the normalisation at  $w = 1$ . The values used are given in Tab. 6.

### A.2. Form factors for $B \rightarrow \pi \ell \nu$

The vector current describing the semileptonic  $B \rightarrow \pi \ell \nu$  decay is given by

$$\langle \pi|V^\mu|B \rangle = \left( (p_B + p_\pi)^\mu - \frac{m_B^2 - m_\pi^2}{t} (p_B - p_\pi)^\mu \right) f_+(t) + \left( \frac{m_B^2 - m_\pi^2}{t} (p_B - p_\pi)^\mu \right) f_0(t), \quad (\text{A.4})$$

Parameter	Value	Parameter	Value
$m_{f_{+1}}^2$	28.40 GeV <sup>2</sup>	$r_{f_{+1}}$	0.744
$m_{f_{+2}}^2$	40.73 GeV <sup>2</sup>	$r_{f_{+2}}$	-0.486
$m_{f_0}^2$	33.81 GeV <sup>2</sup>	$r_{f_0}$	0.258

**Tab. 7** Parameter values used for the transition current  $\langle \pi | V^\mu | B \rangle$  taken from the pole parametrisation in [40].

with form factors parametrised as [40]

$$f_+(t) = \frac{r_{f_{+1}}}{1 - \frac{t}{m_{f_{+1}}^2}} + \frac{r_{f_{+2}}}{1 - \frac{t}{m_{f_{+2}}^2}}, \quad (\text{A.5})$$

$$f_0(t) = \frac{r_{f_0}}{1 - \frac{t}{m_{f_0}^2}}. \quad (\text{A.6})$$

$r_{f_{+1}}$ ,  $r_{f_{+2}}$ , and  $r_{f_0}$  are normalisations and  $m_{f_{+1}}$ ,  $m_{f_{+2}}$ , and  $m_{f_0}$  pole masses. Their values are listed in Tab. 7.

### A.3. Form factors for $B \rightarrow D_0^* \ell \nu$

Parameter	Value	Parameter	Value
$\epsilon_c$	0.3571 GeV <sup>-1</sup>	$\bar{\Lambda}$	0.4 GeV
$\epsilon_b$	0.1042 GeV <sup>-1</sup>	$\bar{\Lambda}^*$	0.75 GeV
$\zeta'$	-1.0	$\zeta(1)$	1.0

**Tab. 8** Parameter values used for the transition current  $\langle D_0^* | A^\mu | B \rangle$  taken from the pole parametrisation in [48, 49].

The axial-vector current describing the semileptonic  $B \rightarrow D_0^* \ell \nu$  decay is given by

$$\langle D_0^* | A^\mu | B \rangle = \sqrt{m_B m_{D_0^*}} (g_+(w)(v_B + v_{D_0^*})^\mu + g_-(w)(v_B - v_{D_0^*})^\mu). \quad (\text{A.7})$$

with the form factors  $g_\pm$  parametrised as [48, 49]

$$g_+(w) = \epsilon_c \left[ 2(w-1)\zeta_1(w) - 3\zeta(w) \frac{w\bar{\Lambda}^* - \bar{\Lambda}}{w+1} \right] - \epsilon_b \left[ \frac{\bar{\Lambda}^*(2w+1) - \bar{\Lambda}(w+2)}{w+1} \zeta(w) - 2(w-1)\zeta_1(w) \right], \quad (\text{A.8})$$

$$g_-(w) = \zeta(w). \quad (\text{A.9})$$

with

$$\zeta(w) = \zeta(1) \times [1 + \zeta'(w-1)], \quad (\text{A.10})$$

$$\zeta_1(w) = \bar{\Lambda} \zeta(w). \quad (\text{A.11})$$

where  $\zeta'$  denotes the form factor slope. The parameters are defined as  $\epsilon_c \equiv \frac{1}{2m_c}$ ,  $\epsilon_b \equiv \frac{1}{2m_b}$ ,  $\bar{\Lambda} \equiv m_D - m_c$ , and  $\bar{\Lambda}^* \equiv m_{D_0^*} - m_c$ . Their values are listed in Tab. 8. As can be seen from the hadronic current of eq. (A.7) the role of vector and axial-vector terms are reversed in decays to scalars as opposed to decays to pseudo-scalars. Thus, in the discussion of IB and SD terms the role of  $V_{\mu\nu}$  and  $A_{\mu\nu}$  are reversed. In particular,  $V_{\mu\nu}^{\text{IB}} = 0$  and  $A_{\mu\nu}^{\text{IB}} \neq 0$ .

## B. Next-to-leading order matrix elements

This appendix presents details on the real emission matrix elements with special focus on the inner bremsstrahlungs (IB) vertex emission terms. The corresponding virtual emission matrix elements can be found in [18], Sec. 4.3. They are calculated in  $D = 4 - 2\epsilon$  dimensions and are UV regularised using the Pauli-Villars prescription [22] of introducing an unphysical heavy photon of mass  $\Lambda$ , the matching scale to the short distance result.

The summed matrix element of the Feynman graphs a to c in Fig. 3 for  $B^+ \rightarrow \bar{X}^0 \ell^+ \nu_\ell \gamma$  is

$$\begin{aligned} \mathcal{M}_1^{\frac{1}{2}} &= i e \frac{G_F}{\sqrt{2}} V_{\text{xb}} H_\mu(p_B, p_X; t) \bar{u}_\nu P_R \gamma^\mu \frac{p_\ell \cdot \epsilon^* + \frac{1}{2} k \not{\epsilon}^*}{p_\ell \cdot k} v_\ell \\ &\quad - i e \frac{G_F}{\sqrt{2}} V_{\text{xb}} \frac{p_B \cdot \epsilon^*}{p_B \cdot k} H_\mu(p_B - k, p_X; t') \bar{u}_\nu P_R \gamma^\mu v_\ell \\ &\quad + \mathcal{M}_{1, \text{vertex emission}}^{\frac{1}{2}}. \end{aligned} \quad (\text{B.1})$$

Similarly, the summed matrix element of the Feynman graphs a to c in Fig. 4 for  $B^0 \rightarrow \bar{X}^- \ell^+ \nu_\ell \gamma$  is

$$\begin{aligned} \mathcal{M}_1^{\frac{1}{2}} &= i e \frac{G_F}{\sqrt{2}} V_{\text{xb}} H_\mu(p_B, p_X; t) \bar{u}_\nu P_R \gamma^\mu \frac{p_\ell \cdot \epsilon^* + \frac{1}{2} k \not{\epsilon}^*}{p_\ell \cdot k} v_\ell \\ &\quad - i e \frac{G_F}{\sqrt{2}} V_{\text{xb}} \frac{p_X \cdot \epsilon^*}{p_X \cdot k} H_\mu(p_B, p_X + k; t') \bar{u}_\nu P_R \gamma^\mu v_\ell \\ &\quad + \mathcal{M}_{1, \text{vertex emission}}^{\frac{1}{2}}. \end{aligned} \quad (\text{B.2})$$

The real emission changes the definition of the four momentum transfer squared, depending on the emission leg:

$$t = (p_B - p_X)^2 = (p_\ell + p_\nu + k)^2, \quad t' = (p_B - p_X - k)^2 = (p_\ell + p_\nu)^2, \quad (\text{B.3})$$

and it is

$$H_\mu(p_1, p_2; t) = (p_1 + p_2)_\mu f_+(t) + (p_1 - p_2)_\mu f_-(t), \quad (\text{B.4})$$

as defined in eq. (2.3). The emission terms off the external mesons and leptons in eqs. (B.1) and (B.2) are, however, not gauge invariant by themselves. The vertex emission terms are thus needed to restore gauge invariance. Assuming  $t = t'$ ,  $f_\pm(t) = f_\pm(t')$ , the vertex emission terms of the constant-form-factor QED invariant Lagrangian of eq. (2.13) are recovered:

$$\mathcal{M}_{1, \text{vertex emission}}^{\frac{1}{2}} = -i e \frac{G_F}{\sqrt{2}} V_{\text{xb}} (f_+(t) + f_-(t)) \bar{u}_\nu P_R \not{\epsilon}^* v_\ell \quad (B^+ \rightarrow \bar{X}^0 \ell^+ \nu_\ell) \quad (\text{B.5})$$

$$\mathcal{M}_{1, \text{vertex emission}}^{\frac{1}{2}} = +i e \frac{G_F}{\sqrt{2}} V_{\text{xb}} (f_+(t) - f_-(t)) \bar{u}_\nu P_R \not{\epsilon}^* v_\ell \quad (B^0 \rightarrow \bar{X}^- \ell^+ \nu_\ell). \quad (\text{B.6})$$

This is a reasonable approximation for heavy meson processes. Here, hard photons are emitted predominantly collinear to the charged lepton. Light meson processes, however, also radiate a considerable fraction of their hard radiation in the direction of the light meson and, hence, give rise to non-negligible corrections for  $t \neq t'$ . There are two ways to obtain these corrections.

**A:** Supposing the form factors  $f_\pm$  can be expanded around  $t$ , the hadronic current reads

$$H_\mu(t') = H_\mu(t) + k' \left. \frac{dH_\mu}{dt} \right|_{k=0} + k'^2 \frac{1}{2} \left. \frac{d^2 H_\mu}{dt'^2} \right|_{k=0} + \mathcal{O}(k^3), \quad (\text{B.7})$$



with  $t' = t + k'$  and  $k' = -2k \cdot (p_B - p_X)$ . Introducing eq. (B.7) into eqs. (B.1) and (B.2) and employing Ward's identity [50] to obtain the gauge restoring terms, results in

$$\begin{aligned} & \mathcal{M}_{1,\text{vertex emission}}^{\frac{1}{2}, B^+ \rightarrow \bar{X}^0 \ell^+ \nu_\ell} \\ &= i e \frac{G_F}{\sqrt{2}} V_{\text{xb}} \bar{u}_\nu P_R \gamma^\mu v_\ell \left( \frac{p_B \cdot \epsilon^*}{p_B \cdot k} k_\alpha - \epsilon_\alpha^* \right) \left( \delta^\alpha_\mu (f_+(t) + f_-(t)) - 2(p_B - p_X)^\alpha \frac{dH_\mu}{dt'} \Big|_{k=0} \right) \\ & \quad + \mathcal{O}(k^2), \end{aligned} \tag{B.8}$$

and

$$\begin{aligned} & \mathcal{M}_{1,\text{vertex emission}}^{\frac{1}{2}, B^0 \rightarrow \bar{X}^- \ell^+ \nu_\ell} \\ &= -i e \frac{G_F}{\sqrt{2}} V_{\text{xb}} \bar{u}_\nu P_R \gamma^\mu v_\ell \left( \frac{p_X \cdot \epsilon^*}{p_X \cdot k} k_\alpha - \epsilon_\alpha^* \right) \left( \delta^\alpha_\mu (f_+(t) - f_-(t)) - 2(p_B - p_X)^\alpha \frac{dH_\mu}{dt'} \Big|_{k=0} \right) \\ & \quad + \mathcal{O}(k^2), \end{aligned} \tag{B.9}$$

respectively. Neglecting higher order terms in the expansion of eq. (B.7) results in Low's matrix element [5] for these processes. This approach, by implying the existence of a Taylor-series representation of the form factors  $f_\pm(t)$ , yields a consistent result both for the interaction terms of the phenomenological Lagrangian and the Feynman rules. However, the exact functional form of the form factors has to be known. Further, by including higher order corrections in  $k$  structure dependent contributions to the matrix element are introduced: the isolated terms that restore gauge invariance are not unique, and undesired ambiguities are apparent. The impact of such terms were studied for  $K_{l3}$  decays in [32, 51], finding negligible impact on the next-to-leading order decay rate. This result however can't be extrapolated to  $B$  meson decays, due to the wide range of possible excited intermediate states.

**B:** A result independent of the functional form of the form factors, and thus not relying on their differentiability, can be derived similarly. Instead of their argument, the form factors themselves are decomposed

$$f_\pm(t') = f_\pm(t) + Z_\pm(t, t'). \tag{B.10}$$

Now, the missing terms for achieving gauge invariance of the real emission amplitude are determined as

$$\begin{aligned} & \mathcal{M}_{1,\text{vertex emission}}^{\frac{1}{2}, B^+ \rightarrow \bar{X}^0 \ell^+ \nu_\ell} \\ &= i e \frac{G_F}{\sqrt{2}} V_{\text{xb}} \bar{u}_\nu P_R \gamma^\mu v_\ell \left( - (f_+(t') + f_-(t')) \epsilon_\mu^* \right. \\ & \quad \left. + (p_B + p_X)_\mu \epsilon^* \cdot Z_+(t, t') + (p_B - p_X)_\mu \epsilon^* \cdot Z_-(t, t') \right) \end{aligned} \tag{B.11}$$

and

$$\begin{aligned} & \mathcal{M}_{1,\text{vertex emission}}^{\frac{1}{2}, B^0 \rightarrow \bar{X}^- \ell^+ \nu_\ell} \\ &= i e \frac{G_F}{\sqrt{2}} V_{\text{xb}} \bar{u}_\nu P_R \gamma^\mu v_\ell \left( (f_+(t') - f_-(t')) \epsilon_\mu^* \right. \\ & \quad \left. + (p_B + p_X)_\mu \epsilon^* \cdot Z_+(t, t') + (p_B - p_X)_\mu \epsilon^* \cdot Z_-(t, t') \right), \end{aligned} \tag{B.12}$$

respectively.  $Z_\pm(t, t') = \frac{k \cdot n}{k \cdot n} Z_\pm(t, t') = k_\alpha \frac{n^\alpha}{k \cdot n} (f_\pm(t') - f_\pm(t)) \equiv k_\alpha Z_\pm^\alpha(t, t')$ ,  $k \cdot n \neq 0$  but otherwise arbitrary. Through the definition of  $n$ , however, again ambiguities are introduced into this generic result which, again, are assumed to be negligible in this paper. The emission terms constructed this way constitute the inner-bremsstrahlung part of non-local emission term  $V_{\mu\nu}^{\text{IB}}$  of Sec. 2.3.

## References

- [1] N. Cabibbo, *Unitary Symmetry and Leptonic Decays*, Phys. Rev. Lett. **10** (1963), 531–533.
- [2] M. Kobayashi and T. Maskawa, *CP Violation in the Renormalizable Theory of Weak Interaction*, Prog. Theor. Phys. **49** (1973), 652–657.
- [3] J. Charles et al., CKMfitter Group collaboration, *CP violation and the CKM matrix: Assessing the impact of the asymmetric B factories*, Eur. Phys. J. **C41** (2005), 1–131, [[hep-ph/0406184](#)].
- [4] M. Bona et al., UTfit collaboration, *The UTfit collaboration report on the status of the unitarity triangle beyond the standard model. I: Model-independent analysis and minimal flavour violation*, JHEP **03** (2006), 080, [[hep-ph/0509219](#)].
- [5] F. E. Low, *Bremsstrahlung of very low-energy quanta in elementary particle collisions*, Phys. Rev. **110** (1958), 974–977.
- [6] D. R. Yennie, S. C. Frautschi and H. Suura, *The Infrared Divergence Phenomena and High-Energy Processes*, Ann. Phys. **13** (1961), 379–452.
- [7] G. Altarelli and G. Parisi, *Asymptotic freedom in parton language*, Nucl. Phys. **B126** (1977), 298–318.
- [8] A. Sirlin, *Current Algebra Formulation of Radiative Corrections in Gauge Theories and the Universality of the Weak Interactions*, Rev. Mod. Phys. **50** (1978), 573.
- [9] A. Sirlin, *Large  $m(W)$ ,  $m(Z)$  Behavior of the  $O(\alpha)$  Corrections to Semileptonic Processes Mediated by  $W$* , Nucl. Phys. **B196** (1982), 83.
- [10] S. Eidelman et al., Particle Data Group collaboration, *Review of particle physics*, Phys. Lett. **B592** (2004), 1.
- [11] A. Sher et al., *New, high statistics measurement of the  $K^+ \rightarrow \pi^0 e^+ \nu$  ( $Ke3$ ) branching ratio*, Phys. Rev. Lett. **91** (2003), 261802, [[hep-ex/0305042](#)].
- [12] T. Alexopoulos et al., KTeV collaboration, *A Determination of the CKM Parameter  $|V_{us}|$* , Phys. Rev. Lett. **93** (2004), 181802, [[hep-ex/0406001](#)].
- [13] T. Alexopoulos et al., KTeV collaboration, *Measurements of KL Branching Fractions and the CP Violation Parameter  $|\eta^\pm|$* , Phys. Rev. **D70** (2004), 092006, [[hep-ex/0406002](#)].
- [14] T. Alexopoulos et al., KTeV collaboration, *Measurements of Semileptonic KL Decay Form Factors*, Phys. Rev. **D70** (2004), 092007, [[hep-ex/0406003](#)].
- [15] E. Barberio, B. van Eijk and Z. Waś, *PHOTOS: A Universal Monte Carlo for QED radiative corrections in decays*, Comput. Phys. Commun. **66** (1991), 115–128.
- [16] E. Barberio and Z. Waś, *PHOTOS - a universal monte carlo for QED radiative corrections: version 2.0*, Comput. Phys. Commun. **79** (1994), 291–308.
- [17] T. C. Andre, *Radiative corrections in  $K0L3$  decays*, Nucl. Phys. Proc. Suppl. **142** (2005), 58–61, UMI-31-49380.

- [18] F. U. Bernlochner and H. Lacker, *Radiative corrections in exclusive semileptonic B-meson decays to (pseudo)scalar final state mesons*, arXiv:1003.1620 [hep-ph].
- [19] T. Gleisberg, S. Höche, F. Krauss, M. Schönherr, S. Schumann, F. Siegert and J. Winter, *Event generation with SHERPA 1.1*, JHEP **02** (2009), 007, [arXiv:0811.4622 [hep-ph]].
- [20] M. Schönherr and F. Krauss, *Soft photon radiation in particle decays in SHERPA*, JHEP **12** (2008), 018, [arXiv:0810.5071 [hep-ph]].
- [21] S. Descotes-Genon and B. Moussallam, *Radiative corrections in weak semi-leptonic processes at low energy: A two-step matching determination*, Eur. Phys. J. **C42** (2005), 403–417, [hep-ph/0505077].
- [22] W. Pauli and F. Villars, *On the Invariant regularization in relativistic quantum theory*, Rev. Mod. Phys. **21** (1949), 434–444.
- [23] T. Kinoshita, *Mass singularities of Feynman amplitudes*, J. Math. Phys. **3** (1962), 650–677.
- [24] T. D. Lee and M. Nauenberg, *Degenerate Systems and Mass Singularities*, Phys. Rev. **133** (1964), B1549–B1562.
- [25] T. H. Burnett and N. M. Kroll, *Extension of the low soft photon theorem*, Phys. Rev. Lett. **20** (1968), 86.
- [26] D. Becirevic and B. Haas,  *$D^* \rightarrow D\pi$  and  $D^* \rightarrow D\gamma$  decays: Axial coupling and Magnetic moment of  $D^*$  meson*, arXiv:0903.2407 [hep-lat].
- [27] J. Gasser, B. Kubis, N. Paver and M. Verbeni, *Radiative  $K(e3)$  decays revisited*, Eur. Phys. J. **C40** (2005), 205–227, [hep-ph/0412130].
- [28] D. Becirevic and N. Kosnik, *Soft photons in semileptonic  $B \rightarrow D$  decays*, arXiv:0910.5031 [hep-ph].
- [29] J. Bijnens, G. Ecker and J. Gasser, *Radiative semileptonic kaon decays*, Nucl. Phys. **B396** (1993), 81–118, [hep-ph/9209261].
- [30] A. A. Poblaguev, *What can be learned from an experimental study of radiative  $K(l3)$  decay?*, Phys. Atom. Nucl. **62** (1999), 975–979.
- [31] V. Cirigliano and D. Pirjol, *Factorization in exclusive semileptonic radiative B decays*, Phys. Rev. **D72** (2005), 094021, [hep-ph/0508095].
- [32] H. W. Fearing, E. Fischbach and J. Smith, *Current algebra, anti- $k_0-l-3$  form-factors, and radiative anti- $k_0-l-3$  decay*, Phys. Rev. **D2** (1970), 542–560.
- [33] F. Krauss, T. Laubrich and F. Siegert, *Simulation of hadron decays in SHERPA*, in preparation.
- [34] S. Catani and M. H. Seymour, *A general algorithm for calculating jet cross sections in NLO QCD*, Nucl. Phys. **B485** (1997), 291–419, [hep-ph/9605323].
- [35] S. Dittmaier, *A general approach to photon radiation off fermions*, Nucl. Phys. **B565** (2000), 69–122, [hep-ph/9904440].

- [36] S. Catani, S. Dittmaier, M. H. Seymour and Z. Trocsanyi, *The dipole formalism for next-to-leading order QCD calculations with massive partons*, Nucl. Phys. **B627** (2002), 189–265, [hep-ph/0201036].
- [37] P. Golonka and Z. Was, *PHOTOS Monte Carlo: A Precision tool for QED corrections in Z and W decays*, Eur. Phys. J. **C45** (2006), 97–107, [hep-ph/0506026].
- [38] B. Aubert et al., BABAR collaboration, *Measurement of  $|V_{cb}|$  and the Form-Factor Slope in  $\bar{B} \rightarrow D\ell^{-}\bar{\nu}$  Decays in Events Tagged by a Fully Reconstructed B Meson*, Phys. Rev. Lett. **104** (2010), 011802, [arXiv:0904.4063 [hep-ex]].
- [39] B. Aubert et al., BABAR collaboration, *Measurement of the  $B^0 \rightarrow \pi^{-}l^{+}\nu$  Form-Factor Shape and Branching Fraction, and Determination of  $|V_{ub}|$  with a Loose Neutrino Reconstruction Technique*, Phys. Rev. Lett. **98** (2007), 091801, [hep-ex/0612020].
- [40] P. Ball and R. Zwicky, *New results on  $B \rightarrow \pi, K, \eta$  decay form factors from light-cone sum rules*, Phys. Rev. **D71** (2005), 014015, [hep-ph/0406232].
- [41] B. Aubert et al., BABAR collaboration, *Measurements of the Semileptonic Decays  $\bar{B} \rightarrow D\ell\bar{\nu}$  and  $\bar{B} \rightarrow D^*\ell\bar{\nu}$  Using a Global Fit to  $DX\ell\bar{\nu}$  Final States*, Phys. Rev. **D79** (2009), 012002, [arXiv:0809.0828 [hep-ex]].
- [42] M. B. Wise, *Chiral perturbation theory for hadrons containing a heavy quark*, Phys. Rev. **D45** (1992), 2188–2191.
- [43] G. Burdman and J. F. Donoghue, *Union of chiral and heavy quark symmetries*, Phys. Lett. **B280** (1992), 287–291.
- [44] T.-M. Yan et al., *Heavy quark symmetry and chiral dynamics*, Phys. Rev. **D46** (1992), 1148–1164.
- [45] M. B. Wise, *Combining chiral and heavy quark symmetry*, hep-ph/9306277.
- [46] A. Buckley, J. Butterworth, L. Lonnblad, H. Hoeth, J. Monk et al., *Rivet user manual*, arXiv:1003.0694 [hep-ph].
- [47] I. Caprini, L. Lellouch and M. Neubert, *Dispersive bounds on the shape of  $\bar{B} \rightarrow D^{(*)}l\bar{\nu}$  form factors*, Nucl. Phys. **B530** (1998), 153–181, [hep-ph/9712417].
- [48] A. K. Leibovich, Z. Ligeti, I. W. Stewart and M. B. Wise, *Semileptonic B decays to excited charmed mesons*, Phys. Rev. **D57** (1998), 308–330, [hep-ph/9705467].
- [49] A. K. Leibovich, Z. Ligeti, I. W. Stewart and M. B. Wise, *Model independent results for  $B \rightarrow D1(2420) l \text{ anti-}\nu$  and  $B \rightarrow D^*2(2460) l \text{ anti-}\nu$  at order  $\Lambda(QCD)/m(c,b)$* , Phys. Rev. Lett. **78** (1997), 3995–3998, [hep-ph/9703213].
- [50] J. C. Ward, *An Identity in Quantum Electrodynamics*, Phys. Rev. **78** (1950), 182.
- [51] E. Fischbach and J. Smith, *Current algebra,  $k$ - $l$ - $3+$  form-factors, and radiative  $k$ - $l$ - $3+$  decay*, Phys. Rev. **184** (1969), 1645–1660.